JACS
JOURNAL OF THE AMERICAN CHEMICAL SOCIETY

ARTICLE

pubs.acs.org/JACS

Water-Dispersible Sugar-Coated Iron Oxide Nanoparticles. An Evaluation of their Relaxometric and Magnetic Hyperthermia Properties

Lenaic Lartigue,[†,‡] Claudia Innocenti,[‡] Thangavel Kalaivani,[§,⊥] Azzam Awwad,[∥] Maria del Mar Sanchez Duque,[†] Yannick Guari,[*,†] Joulia Larionova,[†] Christian Guérin,[†] Jean-Louis Georges Montero,[∥] Véronique Barragan-Montero,[*,∥] Paolo Arosio,[§] Alessandro Lascialfari,[§,⊥,#] Dante Gatteschi,[‡] and Claudio Sangregorio[*,‡,▽]

[†]Institut Charles Gerhardt Montpellier, UMR 5253 CNRS-UM2, Chimie Moléculaire et Organisation du Solide, Université Montpellier II, Place E. Bataillon, 34095 Montpellier Cedex 5, France

[‡]Dipartimento di Chimica, Università di Firenze and INSTM Research Unit, via della Lastruccia 3, 50019 Sesto F.no Firenze, Italy

[§]Dipartimento di Scienze Molecolari Applicate ai Biosistemi, Università degli Studi di Milano and Consorzio INSTM, Milano Unit, I-20134 Milano, Italy

[⊥]Centro S3, CNR-Istituto di Nanoscienze, I-41125 Modena, Italy

[∥]Equipe SyGReM, Institut des Biomolécules Max Mousseron, UMR 5247, CNRS-UM1-UM2, Bâtiment de Recherche Max Mousseron, Ecole Nationale Supérieure de Chimie de Montpellier, 8 Rue de l'Ecole Normale, 34296 Montpellier Cedex, France

[#]Dipartimento di Fisica "A. Volta", Università degli Studi di Pavia, Via Bassi 6, I-27100 Pavia, Italy

[▽]CNR-ISTM, Via C. Golgi 19, I-23310 Milano, Italy

Supporting Information

ABSTRACT: Synthesis of functionalized magnetic nanoparticles (NPs) for biomedical applications represents a current challenge. In this paper we present the synthesis and characterization of water-dispersible sugar-coated iron oxide NPs specifically designed as magnetic fluid hyperthermia heat mediators and negative contrast agents for magnetic resonance imaging. In particular, the influence of the inorganic core size was investigated. To this end, iron oxide NPs with average size in the range of 4−35 nm were prepared by thermal decomposition of molecular precursors and then coated with organic ligands bearing a phosphonate group on one side and rhamnose, mannose, or ribose moieties on the other side. In this way a strong anchorage of the organic ligand on the inorganic surface was simply realized by ligand exchange, due to covalent bonding between the Fe^{3+} atom and the phosphonate group. These synthesized nanoobjects can be fully dispersed in water forming colloids that are stable over very long periods. Mannose, ribose, and rhamnose were chosen to test the versatility of the method and also because these carbohydrates, in particular rhamnose, which is a substrate of skin lectin, confer targeting properties to the nanosystems. The magnetic, hyperthermal, and relaxometric properties of all the synthesized samples were investigated. Iron oxide NPs of ca. 16−18 nm were found to represent an efficient bifunctional targeting system for theranostic applications, as they have very good transverse relaxivity (three times larger than the best currently available commercial products) and large heat release upon application of radio frequency (RF) electromagnetic radiation with amplitude and frequency close to the human tolerance limit. The results have been rationalized on the basis of the magnetic properties of the investigated samples.

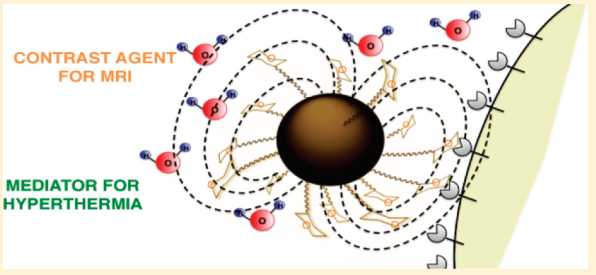

INTRODUCTION

Nanometer-scale magnetic nanoparticles (NPs) have attracted widespread attention due to the rapidly increasing number and variety of their applications in the biomedical sciences, including imaging[1] and therapy.[2] Indeed, they possess unique nanoscale size-dependent physical and chemical properties that can be controlled in a manner that is not possible in the corresponding bulk materials.[3] When these tiny materials are introduced into biological systems, their small size and physicochemical properties enable them to operate as probes and delivery vectors suitable as candidates for the next generation of diagnostic and therapeutic techniques. In this regard, an exciting potential of magnetic NPs resides in the possibility of preparing multifunctional theranostic NPs which may be used as contrast agents (CA) for magnetic resonance imaging (MRI) and

Received: December 20, 2010
Published: May 23, 2011

as heat nanosources to achieve targeted treatment of malignant cells.

Magnetic hyperthermia, which is based on the exothermic properties of magnetic materials under the influence of an alternating current (ac) magnetic field, is a promising cancer thermotherapy. Since the pioneering work of Gilchrist et al.,[4] magnetic hyperthermia has been the aim of numerous in vitro and in vivo studies. In the quest for the most efficient heat mediators several different classes of materials have been investigated such as magnetic nanocomposite microparticles,[5] surface-modified superparamagnetic NPs (ferrofluids)[6] and ligand-targeted magnetoliposomes.[7] Surface-modified super-paramagnetic NPs based on not targeted dextran or carbodextran coated magnetite NPs[8] have been proposed for magnetic fluid hyperthermia (MFH) since the early 1980s in cancer treatment, and successful clinical trials have been performed on human patients in the past decade.[9]

Furthermore, thanks to the capability of iron oxide NPs to enhance proton relaxation at their sites of accumulation[10] and to their high biocompatibility, this kind of material has rapidly become an important tool in the field of contrast enhancement in MRI images applied to the noninvasive diagnosis of many diseases in human soft tissues.[11] During the past 2 decades, super-paramagnetic iron oxides NPs (SPIONs) and ultrasmall-sized super-paramagnetic iron oxides (USPIONs) dispersed in aqueous phase have been investigated to explore their potential as contrast-enhancing probes for MRI. Some of these materials are under clinical evaluation or already used in clinical practice: for instance, Endorem (Guerbet), also called Feridex, Feraheme (AMAG Pharmaceuticals), Primovist and Eovist (Bayer Schering Pharma AG) are used as CAs while other products such as Supravist-SHU555C (Bayer Schering Pharma AG), VSOP-C184 (Ferropharm GmbH), Ferumoxtran-AMI-227 and Ferumoxide-AMI-25 (AMAG Pharmaceuticals) will enter the market soon.[12] Many efforts have also been made to design iron oxide NPs with improved properties in order to decrease the CA concentration, increase the circulation time in the organism, and enhance selective NPs' transport into the cell membrane .[13]

Synthetic chemistry has now developed to a stage where it is possible to produce magnetic NPs for in vivo biomedical applications such as medical imaging and magnetic thermotherapy achieving the so-called "find, fight, and follow" concept of early diagnosis and therapy control. Consequently, NPs may be injected intravenously, utilizing the blood circulation to transport them to their target sites, and their progression in the body may be followed by MRI. After penetrating the tumor cell, its eradication should be achieved for the lowest possible NP concentration. Nevertheless, the difficulty in designing such nanoprobes consists in the fact that they should exhibit remarkable hyperthermal and relaxometric efficiencies at physiological conditions and have adequate biocompatibility and targeting properties. Thus, the use of magnetic NPs for theranostic applications requires better control of the NP core, size, shape, chemical composition, degree of aggregation, and surface state,[14] whereas to ensure the circulation within the living organism, effective vectorization of these nanoprobes is required to direct them toward the desired target allowing a reduction in the total amount of targeted NPs compared with untargeted NPs. Along this line of thought, numerous studies have been devoted to the investigation of iron oxide NPs stabilized with different biocompatible ligands including various polymers,[15] albumin,[16] folic acid,[17] dextran,[18] pluronic,[19] starch,[20] herceptin,[21] nucleic acid molecules (aptamer),[22] peptides (cRGDyK),[23] and others. Further, magnetic iron oxide NPs have been engineered by conjugation with biomolecules to target specific gene expression[24] or to be internalized by cells and thereby to allow cell migration to be monitored in vivo.[11a]

Among the different biocompatible tumor cell-targeting ligands investigated to date, saccharides represent promising molecules for the delivery of such nanoprobes. In fact, they are involved as recognition markers in numerous physiological and pathological processes, mainly occurring on the surfaces of the cell and can be recognized by carbohydrate-binding proteins, such as antibodies, enzymes, and lectins.[25] Very recently, magnetic glycol-NPs based nanosensors bearing carbohydrate ligands were shown to strongly interact with endogenous lectins present on the cancer cell surface.[26] Moreover, membrane-bound receptors, such as lectins, are known to assist material internalization inside the cell via endocytosis following the binding of their ligand.[27] Some examples of saccharide-coated iron oxide NPs have been reported: these include the attachment on Fe_3O_4 NPs of dihydroxyborylphenyl groups functionalized with different mono- and oligosaccharides,[28] the grafting of silica-coated Fe_3O_4 NPs with functionalized D-mannose through a triazol linker,[29] the noncovalent coating of iron oxide NPs with poly(D,L-lactide-*co*-glycoside) via emulsion techniques,[30] or the co-precipitation of iron salts in the presence of D-mannose.[31]

We have recently reported a new approach to achieve size controlled water-dispersible magnetic iron oxide NPs covalently linked to monosaccharide molecules via a phosphonate moiety.[32] These water-dispersible biocompatible rhamnose-coated iron oxide NPs of 4.0 nm were shown to have super-paramagnetic behavior and nuclear relaxivities in the same order of magnitude as Endorem. These characteristics make them potential third generation MRI CAs because the saccharides also represent specific ligands able to target lectins on skin cells. We first focused on rhamnose, as it has been shown that fluorescent rhamnose-coated liposomes could transfer fluorescence from liposomes to skin cells. Moreover, ex vivo experiments on human skin section have demonstrated specific delivery to the epidermis or the horny layer due to the presence of rhamnose ligands on the surface of liposomes.[33] These preliminary results encouraged us to further investigate this approach and to evaluate the potential multifunctional theranostic efficiency of the sugar-coated iron oxide NPs combining the MFH therapeutic action with the MRI diagnostic. To this end, our strategy for the synthesis of NPs was extended to other sugar derivatives of interest, such as mannose which is an efficient vector to target macrophages and hepathic cells[34] and, in order to demonstrate the general applicability of the synthetic methodology, to the pentose derivative, ribose. Further, to investigate the role of the inorganic core, rhamnose-coated iron oxides NPs with various sizes in the range of 4−35 nm were synthesized and their magnetic, relaxometric, and hyper-thermal properties systematically studied.

EXPERIMENTAL SECTION

Nanoparticle Labeling. Molecules derived from carbohydrates bearing ester phosphonate groups were referred to as **Rha** for rhamnose, **Man** for mannose, and **Rib** for ribose (see Schemes 1 and 2). The iron oxide NPs functionalized with these ligands are named as follows: the prefix **Rha**, **Man**, or **Rib** denotes the type of carbohydrate derivative grafted on the surface of the nanoparticles of ca. 4, 7, 10, 16, 18, or 35 nm. As an example, **Rha-4** denotes iron oxide nanoparticles of 4 nm in size grafted with the rhamnose derivative. Thus, we obtained a

Scheme 1. Synthesis of the Rhamnose Derivative Functionalized at the Anomeric Position, Rha_{AC}

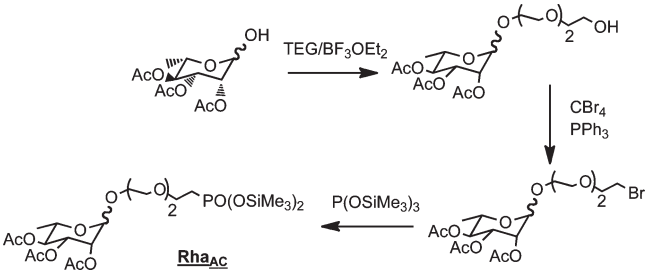

Scheme 2. Phosphonate-Functionalized Sugars Rha_{AC}, Man_{AC}, and Rib_{AC}

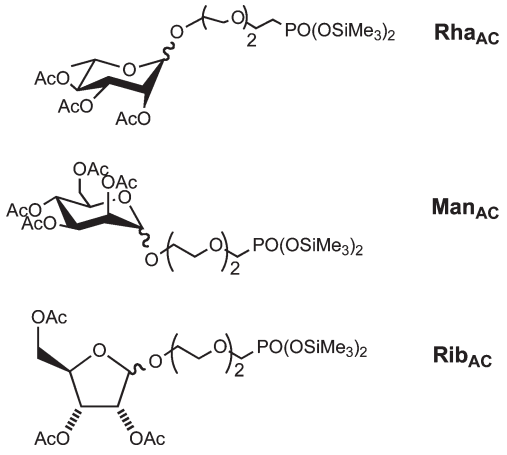

series of iron oxide nanoparticles of varying size (4−35 nm) bearing different sugars, which are **Rha-4**, **Man-4**, **Rib-4**, **Rha-7**, **Rha-10**, **Rha-16**, **Rha-18**, and **Rha-35**.

Synthesis. The syntheses were carried out using standard anaerobic procedures and commercially available reagents. Absolute ethanol, hexane, methanol, and dichloromethane (99%) were used as received. Tetrahydrofuran, THF, was purified by distillation over sodium. 1,2-Hexadecanediol (90%), oleic acid (90%), 2.0 M ammonia solution in methanol, iron(III) oxide hydrated catalyst grade 30−50 mesh, docosan (99%), tris(trimethylsilyl)phosphate, triethylene glycol (TEG), boron trifluoride etherate, tetrabromomethane, and triphenylphosphite were purchased from Aldrich Chemical Co. Phenyl ether (99%), oleylamine approximate C18 content 80−90% (97%), and iron(III) acetylacetonate (99+%) were purchased from Acros Organics. 1-Methylpyrrole (99%) was purchased from Alfa Aesar. Rhamnose, mannose, and ribose were purchased from Benn Chemicals.

*Synthesis of the Rhamnose Derivative (**Rha_{AC}**). Synthesis of 2-[2-(2-Hyroxyethoxy)ethoxy]ethyltri-O-acetylrhamnopyranoside.* A 90.35 mmol amount of boron trifluoride etherate was added dropwise at 0 °C to 18.07 mmol of L-(+)-rhamnose pentaacetate dissolved in dichloromethane (14 mL) and 54.21 mmol of triethylene glycol. The mixture was magnetically stirred under argon, at 0 °C for 15 min, and then under ambient conditions overnight. The mixture was diluted in dichloromethane (25 mL) and then washed (2 × 25 mL of water, 2 × 25 mL of a solution of 5% sodium bicarbonate, and 2 × 25 mL of water). The organic layer was dried over anhydrous sodium sulfate, filtered, and concentrated in vacuo. The residue was chromatographed on silica gel (dichloromethane/methanol, 9/1) to give the expected compound in 64% yield. R_f = 0.52 (CH_2Cl_2/MeOH, 95/5). $[\alpha]_D$: −38.2 (c = 1.03, $CHCl_3$). SM (ESI > 0/MeOH/30 eV): m/z 445.32 $[M + Na]^+$ ^{1}H. NMR (400 MHz, $CDCl_3$; ppm): δ 1.18 (3H, d, J_{6-5} = 6,3 Hz, CH−CH_3), 1.95, 2.01, 2.11 (9H, 3s, CH_3CO), 3.57−3.71 (12H, m, CH_2−O), 3.89 (1H, dd, J_{5-4} = 9.8 Hz, J_{5-6} = 6.3 Hz, CH−CH$_3$), 4.75 (1H, d, J_{1-2} = 1.7 Hz, O−CH−O), 5.03 (1H, dd, J_{4-5} = 9.9 Hz, J_{4-3} = 9.9 Hz, CH$_3$−CH−CH), 5.22 (1H, dd, J_{2-3} = 3.5 Hz, J_{2-1} = 1.7 Hz, CH−CH−O), 5.27 (1H, dd, J_{3-4} = 10.1 Hz, J_{3-2} = 3.5 Hz, CH$_3$−CH−CH−CH). ^{13}C NMR (100.6 MHz, $CDCl_3$; ppm): δ 17.3 (CH−CH_3), 20.6, 20.7, 20.8 (COCH_3), 61.7 (C−CH_2O), 66.3 (C−CH_2O), 67.1 (C−CH_2O), 69.0 (CH−CH_3), 69.8, 70.0, 70.3 (C−CH_2O), 70.7 (CH−CH−O), 71.0 (CH$_3$−CH−CH−CH), 72.5 (CH$_3$−CH−CH), 97.5 (O−CH−O), 169.9, 170.0, 170.1 (COCH_3).

Synthesis of 2-[2-(2-Bromoethoxy)ethoxy]ethyl-2,3,4,-tri-O-acetylrhamnopyranoside. A 4.02 mmol amount of 2-[2-(2-hydroxyethoxy)-ethoxy]ethyltri-*O*-acetylrhamnopyranoside and 4.82 mmol (1.2 equiv) of tetrabromomethane were dissolved in dichloromethane (20 mL) before adding 5.63 mmol (1.4 equiv) of triphenylphosphine. The mixture was magnetically stirred under argon at room temperature for 150 min. The mixture was diluted in dichloromethane (50 mL), then washed (2 × 50 mL of brine), and dried over anhydrous sodium sulfate, filtrated, and concentrated in vacuo. The residue was chromatographed on silica gel (ether) to give the expected compound in 92% yield. SM (ESI > 0/MeOH/30 eV): m/z 507.29 and 509.2 $[M + Na]^+$. ^{1}H NMR (400 MHz, $CDCl_3$; ppm): δ 1.14 (3H, d, J_{6-5} = 6.3 Hz, CH−CH_3), 1.91, 1.98, 2.08 (9H, 3s, CH_3CO), 3.39−3.43 (2H, m, CH_2−Br), 3.56−3.77 (10H, m, CH_2−O), 3.86 (1H, dd, J_{5-4} = 9.9 Hz, J_{5-6} = 6.4 Hz, CH−CH$_3$), 4.71 (1H, d, J_{1-2} = 1.5 Hz, O−CH−O), 4.99 (1H, dd, J_{4-5} = 9.8 Hz, J_{4-3} = 9.8 Hz, CH$_3$−CH−CH), 5.18 (1H, dd, J_{2-3} = 3.5 Hz, J_{2-1} = 1.8 Hz, CH−CH−O), 5.23 (1H, dd, J_{3-4} = 10.1 Hz, J_{3-2} = 3.6 Hz, CH$_3$−CH−CH−CH). ^{13}C NMR (100.6 MHz, $CDCl_3$; ppm): δ 17.3 (CH−CH_3), 20.6, 20.7, 20.8 (COCH_3), 30.3 (CH_2−Br), 63.4 (C−CH_2O), 66.1 (C−CH_2O), 67.0 (C−CH_2O), 68.9 (CH−CH_3), 69.9, 70.4 (C−CH_2O), 70.6 (CH_2−CH−O), 70.9 (CH$_3$−CH−CH−CH), 71.0 (CH$_3$−CH−CH), 97.4 (O−CH−O), 169.7, 169.8, 169.9 (COCH_3).

*Synthesis of Bis(trimethysilyl)[2-{2-[2-(2,3,4-tri-O-acetylrhamnopyranosyl)oxy]ethoxy}ethyl]phosphonate (**Rha_{AC}**).* A 17.32 mmol (4 equiv) amount of tris(trimethylsilylphosphite) was added to 4.33 mmol of 2-[2-(2-bromoethoxy)ethoxy]ethyl-2,3,4,-tri-*O*-acetylrhamnopyranoside under argon. The mixture was magnetically stirred under argon at 140 °C for 5 h. The tris(trimethylsilylphosphite) was then removed under vacuum to give the expected compound in quantitative yield. ^{1}H NMR (400.0 MHz, $CDCl_3$; ppm): δ 0.23 (18H, m, Me_3Si), 1.18 (3H, d, J = 6.3 Hz, CH−CH_3), 1.95, 2.05, 2.13 (9H, 3s, CH_3CO), 2.07−2.12 (2H, m, CH_2−P), 3.63−3.78 (10H, m, O−CH_2), 3.98 (1H, dd, J = 9.6 Hz, J = 6.1 Hz, CH$_3$−CH), 4.82 (1H, s, O−CH−O), 5.00 (1H, dd, J = 9.6 Hz, J = 9.9 Hz, CH$_3$−CH−CH), 5.23 (2H, m, CH−CH−CH−CH). ^{13}C NMR (100.6 MHz, $CDCl_3$; ppm): δ 15.5 (CH$_3$−CH), 18.8−18.9−19.0 (COCH_3), 63.5 (CH_2−P), 64.4 (CH$_3$−CH), 65.2 (C−CH_2O), 67.9−67.1 (CH$_3$−CH−CH−CH), 68.1−68.2, 68.6−68.7 (C−CH_2O), 69.2 (O−CH−CH), 95,6 (O-CH−O), 168.0−168.1−168.2 (COCH_3). For hydrolyzed product: SM (ESI > 0/MeOH/30 eV): m/z 509.24 $[M + H]^+$. $[\alpha]_D$: −27.1 (c = 1, MeOH).^{31}P NMR (81.0 MHz, $CDCl_3$; ppm): δ 22.4.

*Synthesis of the Mannose Derivative (**Man_{AC}**). Synthesis of 2-[2-(2-Hydroxyethoxy)ethoxy]ethyltetra-O-acetylmannopyranoside.* A methodology similar to the synthesis of 2-[2-(2-hydroxyethoxy)ethoxy]ethyltri-*O*-acetylrhamnopyranoside utilized 64.1 mmol of boron trifluoride etherate, 12.8 mmol of D-mannose tetraacetate, and 38.4 mmol of triethylene glycol to give the expected compound in 78% yield. SM (ESI > 0/MeOH/30 eV): m/z 503.22 $[M + Na]^+$. R_f (5/5 AcOEt/EP, v/v) = 0.45. ^{1}H NMR (400 MHz, $CDCl_3$; ppm) δ 1.99−2.04, 2.10−2.16 (12H, 4s, CH_3CO), 3.61−3.84 (m, 11H, CH_2CH_2O), 4.09−4.12 (3H, m, AcO−CH_2-b, CH−CH$_2$−OAC, 1 CH−O−CH_2),

4.26−4.3 (1H, dd, AcO−CH_2-a), 4.88 (1H, s, O−C*H*−O), 5.27 (1H, dd, CH_2−CH−C*H*), 5.30 (1H, dd, O−CH−C*H*), 5.35 (1H, dd, O−CH−CH−C*H*). ^{13}C NMR (100.6 MHz, $CDCl_3$; ppm): δ 20.7, 20.8, 20.9 ($COCH_3$), 61.8 (*C*−CH_2O), 62.4 (CH−*C*H_3), 66.2 (*C*−CH_2O), 67.4 (*C*−CH_2O), 68.4 (CH_3−CH−CH−*C*H), 69.1 (*C*H−CH_3), 69.6, 70.0, 70.4 (*C*−CH_2O), 70.8 (*C*H−CH−O), 72.6 (CH_3−CH−*C*H), 97.7 (O−*C*H−O), 169.8, 170.0, 170.1, 170.7 (*C*OCH_3).

Synthesis of 2-[2-(2-Bromoethoxy)ethoxy]ethyltetra-O-acetylmannopyranoside. A methodology similar to the synthesis of 2-[2-(2-bromoethoxy)ethoxy]ethyltri-*O*-acetylrhamnopyranoside utilized 10 mmol of 2-[2-(2-(hydroxyethoxy)ethoxy]ethyltetra-*O*-acetylmannopyranoside, 12 mmol (1.2 equiv) of tetrabromomethane and 14 mmol (1.4 equiv) of triphenylphosphite to give the expected compound in 87% yield. SM (ESI > 0/MeOH/30 eV): *m*/*z* 565.25, 567.22 $[M + Na]^+$. ^{1}H NMR (400 MHz, $CDCl_3$; ppm): δ 1.92−1.98, 2.04−2.10 (12H, 4s, CH_3CO), 3.4 (2H, t, CH_2Br), 3.6−3.77 (m, 9H, CH_2CH_2O), 3.98−4.06 (3H, m, AcO−CH_2-b, C*H*−CH_2−OAc, 1 CH−O-CH_2), 4.2−4.25 (1H, dd, AcO−CH_2-a), 4.81(1H, s, O−C*H*-O), 5.2−5.24 (1H, t, CH_2−CH−C*H*), 5.2 (1H, d, O−CH−C*H*), 5.27−5.3 (1H, dd, O−CH−CH−C*H*). ^{13}C NMR (100.6 MHz, $CDCl_3$; ppm): δ 20.7, 20.8, 20.9 ($COCH_3$), 30.4 (CH_2−Br), 62.4 (CH−*C*H_3), 66.2 (*C*−CH_2O); 67.4 (*C*−CH_2O), 68.4 (CH_3−CH−CH−*C*H), 69.1 (*C*H−CH_3), 69.6, 70.1, 70.6 (*C*-CH_2O), 70.7 (*C*H−CH−O), 71.2 (CH_3−CH−*C*H), 97.7 (O−*C*H−O), 169.7, 169.9, 170.1, 170.7 (*C*OCH_3).

*Synthesis of Bis(trimethylsilyl)[2-(2-{2-[(2,3,4,6-tetra-O- acetylmannopyranosyl)oxy]ethoxy}ethoxy)ethyl]phosphonate (**Man$_{AC}$**).* A methodology similar to the synthesis of bis(trimethylsilyl)[2-(2-{2-[-(2,3,4-tri-*O*-acetylrhamnopyranosyl)oxy]ethoxy}ethylphosphonate utilized 19.68 mmol (4 equiv) of tris(trimethylsilylphosphite) and 3.68 mmol of 2-[2-(2-bromoethoxy)ethoxy]ethyltri-*O*-acetylrhamnopyranoside to give the expected compound in quantitative yield. R_f (Et_2O 100%) = 0.6. ^{1}H NMR (400 MHz, $CDCl_3$; ppm): δ 0.23 (18H, m, Me_3Si,), 1.92−1.98, 2.04−2.10 (12H, 4s, CH_3CO), 2.07−2.12 (2H, m, CH_2P), 3.6−3.77 (9H, m, CH_2CH_2O), 3.98−4.06 (m, 3H, AcO−CH_2-b, C*H*−CH_2−OAc, 1 CH−O−CH_2), 4.2−4.25 (dd, 1H, AcO−CH_2-a), 4.81(s, 1H, O−C*H*−O), 5.2−5.24 (t, 1H, CH_2−CH−C*H*), 5.2 (d, 1H, O−CH−C*H*), 5.27−5.3 (dd, 1H, O−CH−CH−C*H*). ^{13}C NMR (100.6 MHz, $CDCl_3$; ppm): δ 20.7, 20.8, 20.9 ($COCH_3$), 62.4 (CH−*C*H_3), 65.4 (*C*H_2−P), 65.8 (CH_3−CH−*C*H), 66.2 (*C*−CH_2O), 67.4 (*C*−CH_2O), 68.4 (CH_3−CH−CH−*C*H), 69.1 (*C*H−CH_3), 69.6, 70.0, 70.1 (*C*−CH_2O), 70.5 (*C*H−CH−O), 97.7 (O−*C*H−O), 169.7, 169.8, 170.0, 170.6 (*C*OCH_3). For hydrolyzed product SM (ESI > 0/MeOH/30 eV): *m*/*z* 567.45 $[M + Na]^+$. ^{31}P NMR (81.0 MHz, $CDCl_3$; ppm): δ 22.4.

*Synthesis of the Ribose Derivative (**Rib$_{AC}$**). Synthesis of 2-[2-(2-Hydroxyethoxy)ethoxy]ethyl-2,3,5-tri-O-acetylribofuranoside.* A methodology similar to the synthesis of 2-[2-(2-hydroxyethoxy)-ethoxy]ethyltri-*O*-acetylrhamnopyranoside utilzied 78.61 mmol of boron trifluoride etherate, 15.72 mmol of acetylated ribose, and 47.16 of triethylene glycol to give the expected compound in 51% yield. SM (ESI > 0/MeOH/30 eV): *m*/*z* 431.15 $[M + Na]^+$. ^{1}H NMR (400 MHz, $CDCl_3$; ppm): δ 2.18−2.21 (9H, t, CH_3−CO-), 3.54−3.67 (12H, m, CH_2CH_2O), 4.09−4.13 (1H, dd, AcO−CH_2−C*H*), 4.18−4.22 (2H, m, AcO−CH_2−CH), 4.26−4.31 (2H, m, C*H*−OAc), 5.05 (0.6H, s, O−C*H*α−O), 5.22 (0.4H, s, O−C*H*β−O), 2.21−2.30 (9H, m, O−CH_3). ^{13}C NMR (100.6 MHz, $CDCl_3$; ppm): δ 20.5−21.0−21.3 (CH_3−CO-), 61.4 (*C*−CH_2OH), 62.4 (CH−*C*H_2), 67.1 (*C*−CH_2O), 70.0 (*C*H_2−OAc), 70.1−70.4−70.8 (*C*−CH_2O), 71.9 (CH_2−OH), 73.0 (*C*H_2−OAc), 82.8 (*C*H−CH_2−OAc), 102.0 (O−*C*H−O), 169.9−170.1−170.4 (C═O).

Synthesis of 2-[2-(2-Bromoethoxy)ethoxy]ethyl-2,3,5-tri-O-acetylribofuranoside. A methodology similar to the synthesis of 2-[2-(2-bromoethoxy)ethoxy]ethyltri-*O*-acetylrhamnopyranoside utilized 6.21 mmol of 2,3,5-tri-*O*-acetyl-α-ribofuranoside of 3′,6′,8′-trioxanonanyle, 7.45 mmol (1.2 equiv) of tetrabromomethane, and 8.7 mmol (1.4 equiv) of triphenylphosphite to give the expected compound in 90% yield. SM (ESI > 0/MeOH/30 eV): *m*/*z* 493.07 $[M + Na]^+$. ^{1}H NMR (400 MHz, $CDCl_3$; ppm): δ 2.20−2.28 (9H, m, O−CH_3), 3.52−3.66 (12H, m, CH_2CH_2O), 4.10−4.14 (1H, dd, AcO−CH_2−C*H*), 4.18−4.22 (2H, m, AcO−CH_2−CH), 4.25−4.30 (2H, m, C*H*−OAc), 5.01 (0.6H, s, O−C*H*α−O), 5.19 (0.4H, s, O−C*H*β−O). ^{13}C NMR (100.6 MHz, $CDCl_3$; ppm): δ 21.1−21.3−21.5 (H_3C−CO), 61.7 (*C*−CH_2OH), 62.4 (CH−*C*H_2), 67.1 (*C*−CH_2O), 70.1 (*C*H_2−OAc), 70.1−70.4−70.9 (*C*−CH_2O), 72.6 (*C*H_2−Br), 73.2 (CH_2−OAc), 84.5 (*C*H−CH_2−OAc), 108.0 (O−*C*H−O), 107.2−107.4, 107.5 (*C*═O).

*Synthesis of Bis(trimethylsilyl)[2-(2-{2-[(2,3,5-tri-O-acetylribofuranosyl)oxy]ethoxy}ethoxy)ethyl]phosphonate (**Rib$_{AC}$**).* A methodology similar to the synthesis of bis(trimethylsilyl)[2-(2-{2-[(2,3,4-tri-*O*-acetylrhamnopyranosyl)oxy]ethoxy}ethylphosphonate] utilized 14.4 mmol (4 equiv) of tris(trimethylsilylphosphite) and 3.6 mmol of 2-[2-(2-bromoethoxy)ethoxy]ethyl-2,3,5-tri-*O*-acetylribofuranoside to give the expected compound in quantitative yield. For the hydrolyzed product SM (ESI > 0/MeOH/30 eV): *m*/*z* 495.31 $[M + Na]^+$. ^{1}H NMR (400 MHz, $CDCl_3$; ppm): δ 2,22−2.29 (9H, m, O−CH_3), 3.52−3.60 (10H, m, CH_2CH_2O), 5.42−5.45 (1H, dd, AcO−CH_2−C*H*), 4.18−4.22 (2H, m, AcO−CH_2−CH), 4.85−5.20 (2H, m, C*H*−OAc), 5.54 (0.6H, s, O−C*H*α−O), 5.63 (0.4H, s, O−C*H*β−O). ^{13}C NMR (100.6 MHz, $CDCl_3$; ppm): δ 21.2−21.4−21.6 (H_3C−CO), 38.3(-$CH_2PO_3H_2$), 55.2 (CH_2−CH_2−PO_3H_2), 62.2 (CH−*C*H_2), 69.5−70.3−70.8, 71 (*C*−CH_2O), 73.2 (*C*H_2−OAc), 80.9 (*C*−CH_2O), 84.5 (*C*H−CH_2−OAc), 108.0 (O−*C*H−O), 107.4−107.6−107.8 (*C*═O). ^{31}P NMR (81.0 MHz, $CDCl_3$; ppm): δ 9.21.

General Procedure for Sugar-Coated NPs. Oleic acid-/oleylamine-coated NPs with sizes of ca. 4,[14b] 7,[35] and 10 nm [14m] and oleic acid-coated NPs with sizes of ca. 16,[36] 18,[36] and 35 nm[35] NPs were performed according to published procedures. The coating of the NPs with different sugars was performed according to the procedure described below:

First Step. In a typical experiment, 0.46 mmol of oleic acid-/oleylamine-coated iron oxide nanoparticles and 0.78 mmol of sugar were dissolved in anhydrous THF (5 mL). The mixture was magnetically stirred under argon to reflux for 24 h. Pentane (30 mL) was added to the mixture at room temperature, and the solution was precipitated and separated via centrifugation. The product was dissolved, and centrifugation (120 000 rpm, 10 min) was applied to remove undispersed residue. The solution was precipitated with ethanol (40 mL), and organic compound was removed via centrifugation.

For mannose-coated NPs (Man_{AC}-4). IR: 2925, ν_{as}(C−H); 2856, ν_s(C−H); 1747, ν(COO); 1226, ν(CO); 1080, ν(COC); 1051, $\nu(CH_{cycle})$; 1015, ν(P−O−Fe); 984, ν(P−O−Fe); 588, ν(Fe−O).

For ribose-coated NPs (Rib_{AC}-4). IR: 2925, ν_{as}(C−H); 2872, ν_s(C−H); 1750, ν(COO); 1228, ν(CO); 1084, ν(COC); 1049, $\nu(CH_{cycle})$; 1013, ν(P−O−Fe); 976, ν(P−O−Fe); 598, ν(Fe−O).

For rhamnose-coated NPs (Rha_{AC}-4). IR: 2925, ν_{as}(C−H); 2856, ν_s(C−H); 1747, ν(COO); 1226, ν(CO); 1080, ν(COC); 1051, $\nu(CH_{cycle})$; 1015, ν(P−O−Fe); 984, ν(P−O−Fe); 588, ν(Fe−O).

Second Step. A 0.2 mmol amount of the NPs obtained in the first step was dissolved in a solution of 2 M ammonia methanol (10 mL). The solution was magnetically stirred under argon at room temperature for 4 h. Dichloromethane (30 mL) was then added to the mixture, and the solution was precipitated and separated via centrifugation. The product was dissolved, and centrifugation (120 000 rpm, 10 min) was applied twice to remove organic compounds.

For **Man-4**. Anal. Found (% wt): Fe, 38.27; P, 5.12. IR: 3383 and 3199, ν(OH); 2921, ν_{as}(C−H); 2852, ν_s(C−H); 1243, ν(CO); 1095, ν(COC); 1058, $\nu(CH_{cycle})$; 1015, ν(P−O−Fe); 976, ν(P−O−Fe); 590, ν(Fe−O).

For **Rib-4**. Anal. Found (% wt): Fe, 39.87; P, 4.99. IR: 3425 and 3183, ν(OH); 2922, ν_{as}(C−H); 2856, ν_s(C−H); 1235, ν(CO); 1086, ν-(COC); 1033, $\nu(CH_{cycle})$; 1001, ν(P−O−Fe); 581, ν(Fe−O).

For **Rha-**$_{coated}$. Anal. Found (% wt): (**Rha-4**) Fe, 41.87; P, 4.34; (**Rha-7**) Fe, 48.71; P, 3.87; (**Rha-10**) Fe, 29.21; P, 5.01; (**Rha-16**) Fe, 50.11; P, 3.82; (**Rha-18**) Fe, 49.62; P, 3.72; (**Rha-35**) Fe, 61.23; P, 2.62. IR: 3377 and 3228, ν(OH); 2923, ν_{as}(C−H); 2868, ν_s(C−H); 1245, ν(CO); 1090, ν(COC); 1052, ν(CH$_{cycle}$); 1014, ν(P−O−Fe); 987, ν-(P−O−Fe); 584, ν(Fe−O).

Rhamnose−Phosphonate Leaching Studies for Rha-4. Rhamnose−phosphonate leaching studies from iron oxide NPs were performed on **Rha-4** in water for physiological conditions (pH = 7.4): 5.8 mg of **Rha-4** was solubilized in 50 mL of water (0.649 mmol/L in iron), and the solution was sonicated for 10 min. Then, the NPs were precipitated by adding ethanol and washed thoroughly with the same solvent. This procedure was repeated twice. The IR spectra of the resulting NPs are unchanged, and the Fe/P ratio from elemental and EDX analyses is shown to be unchanged with a value of 87:13, demonstrating the strong anchorage of the organic rhamnose−phosphonate moieties at the NPs surface.

Physical Measurements. ^{1}H, ^{13}C, and ^{31}P NMR spectra were recorded using a Brüker AC-400 spectrometer. Chemical shift values (δ) are reported in parts per million from internal standard tretramethylsilane. Coupling constants (J) are measured in hertz. Multiplicity is reported as follows: s (singlet), d (doublet), t (triplet), m (multiplet), and combination of this signal. Optical rotations were recorded with a Perkin-Elmer 241 polarimeter. Fast atom bombardment mass spectra (FAB-MS) were recorded in positive mode using a JEOL DX 300 spectrometer using NOBA (nitrobenzylic alcohol) as matrix. Column chromatographies were performed on silica gel 60. Dynamic light scattering (DLS) measurements were recorded with a Malvern high-performance particle sizer. IR spectra were recorded using a Perkin-Elmer 1600 spectrometer at 4 cm^{-1} resolution. The surface composition was monitored by X-ray photoelectron spectroscopy (XPS) on an ESCALAB 250 (Thermo Electron). The X-ray excitation was provided by a monochromatic Al Kα (1486.6 eV) source. The diameter of the analyzed surface was 400 μm. The background signal was removed using the Shirley method. The surface atomic concentrations were determined from photoelectron peak areas using the atomic sensitivity factors reported by Scofield. Binding energies (BE) of all core levels were referred to the C−C of C1s carbon at 284.8 eV. Elemental analyses were performed by the Service Central d'Analyze (CNRS, Vernaison, France). The samples were heated at 3000 °C under He. Oxygen was transformed in CO and detected by using an IR detector. Iron was determined by using the emission spectroscopy technique PLASMA ICP. An evaluation of the Fe/P ratio was also performed by using an environmental secondary electron microscope FEI Quanta 200 FEG coupled with an electron dispersive spectroscope Oxford INCA detector. Powder X-ray diffraction patterns were measured with a PanAnalytical diffractometer equipped with an ultrafast X'celerator detector X'pert Pro with nickel-filtered copper radiation (1.5405 Å) and a Bruker D8 Advance diffractometer equipped with Cu Kα radiation and operating in $\theta-2\theta$ Bragg−Brentano geometry at 40 kV and 40 mA. Magnetic susceptibility data were collected with a Quantum Design MPMS-XL SQUID magnetometer working in the temperature range of 1.8−350 K and the magnetic field range of 0−5 T. Data were not corrected for the diamagnetic contribution because, when measured separately, it was found to be negligible with respect to the sample signals. All magnetic measurements were performed on dry powders except when indicated. The samples were pressed into pellets in order to prevent nanocrystal orientation under the external magnetic field. Samples for transmission electron microscopy measurements were prepared by depositing the NPs on carbon-coated copper grids. The measurements were carried out with a microscope JEOL 1200 EXII operated at 100 kV. NMR data were collected by using two different pulsed FT-NMR spectrometers: (i) a Smartracer Stelar relaxometer (with the use of fast-field-cycling technique) for frequencies in the range of 10 kHz ≤ ν ≤ 10 MHz, and (ii) a Stelar Spinmaster for ν > 10 MHz. Standard radio frequency excitation pulse sequences CPMG- (T_2) and saturation-recovery (T_1) were used. From the measured T_1 and T_2 values we have calculated the longitudinal and transverse relaxivities using the usual formula: $r_i = [(1/T_i)_{meas} - (1/T_i)_{dia}]/c$ (i = 1, 2), where $(1/T_i)_{meas}$ is the value measured for the sample of magnetic center concentration c (mmol L^{-1}) and $(1/T_i)_{dia}$ refers to the nuclear relaxation rate of the diamagnetic host solution. GIBCO ultrapure water DNase RNase Free Invitrogen was used for the preparation of two buffer solutions. The first one is 50 mL of 10 mM Hepes and the second 50 mL of 1 M Trima. These two solutions were mixed to obtain an aqueous solution at pH = 7.4. The concentrations were 0.558, 0.218, 0.051, and 0.186 mmol L^{-1} of Fe, respectively, for samples **Rha-4**, **Rha-7**, **Rha-10**, and **Rha-18**. The evaluation of heat generation was performed with an in-house-built magnetothermal setup based on a Nova Star 5 kW (Ameritherm Inc.) generator. A solution of coated magnetic NPs was put in a thermal insulating support inside a coil and the temperature was measured with a VR18_CR digital temperature recorder (Ceam Group) connected to an optical fiber directly dipped into the sample. Although the system is optimized for working in adiabatic conditions, temperature dissipation with the surrounding air was observed. Ultrapure Milli-Q water (Millipore Inc.), minimum resistivity of 18 MΩ, was used to solubilize the NPs. The concentration was 21 g/L for **Rha-4**, 21 g/L for **Rha-7**, 28 g/L for **Rha-10**, 6 g/L for **Rha-16**, and 21 g/L for **Rha-35**. The measurements were performed on 0.3 g of these solutions.

RESULTS AND DISCUSSION

Synthesis and Characterization. The synthesis of iron oxide NPs coated with carbohydrates was carried out using iron oxide NPs, stabilized by oleic acid or a mixture of oleic acid/oleylamine, by the displacement of the stabilizing agents, and by covalent grafting of the carbohydrate derivatives via the phosphonate function.

The synthesis of the rhamnose derivative functionalized at the anomeric position, **Rha$_{AC}$**, depicted in Scheme 1, was carried out in three steps, leading mainly to the α-anomer (95/5). The reaction is constrained to start at the anomeric position by selectively deprotecting the sugar at this site.

The hydroxyl protection was obtained by the action of acetic anhydride in pyridine. The selective deprotection of the anomeric position was achieved by use of hydrazinium acetate.[37] The glycosylation of the deprotected sugar, by the TEG moiety, was obtained in an excellent yield using boron trifluoride as catalyst. Primary alcohol was then halogenated by the couple triphenylphosphine/carbon tetrachloride and an Arbuzov reaction with the sorting trimethylsilyl phosphite[38] led to the desired phosphonate. A similar methodology was applied for the synthesis of the mannose **Man$_{AC}$** and ribose **Rib$_{AC}$** derivatives functionalized at the anomeric position, leading to mainly the α-anomer for the mannose and the β-anomer for the ribose (see Scheme 2).

The postsynthetic anchorage of the phosphonate-functionalized sugars at the surface of the iron oxide NPs was performed in THF by heating for 24 to 48 h. The deprotection of the acetate groups was performed in a methanol/ammonia mixture. The synthesis of the NPs coated with the rhamnose derivative is shown as an example in Scheme 3.

It is noteworthy that while the starting NPs are nonsoluble in methanol and water, they become soluble in methanol but not water when coated with acetate-protected sugar, and then become fully soluble in water after sugar deprotection, as expected considering the different organic groups covering the NPs surface at each step. By following this procedure to synthesize the coated NPs, the sugar

Scheme 3. Synthesis of the Rhamnose-Coated Iron Oxide NPs Rha-4−Rha35

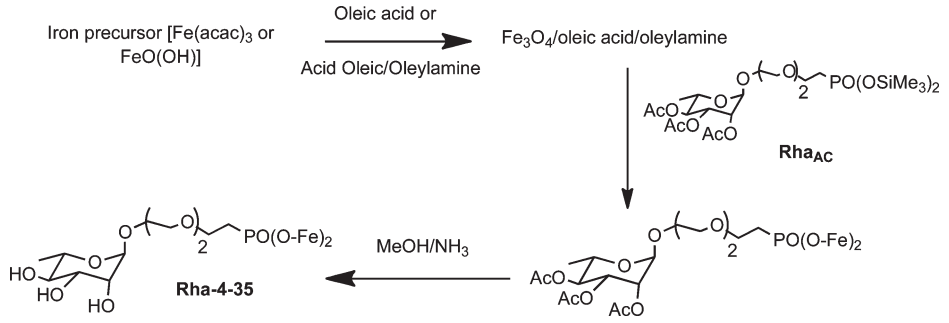

moiety is proposed to be covalently bound to the iron oxide NPs via the phosphonate moiety, which precludes sugar leaching and consequently formation of uncoated iron oxide NPs in the living organism. Such assessment was tested by intense sonication of an aqueous solution of **Rha-4** at physiological pH followed by precipitation and intense washing in order to remove all improperly anchored organic molecules from the NPs surface. IR analysis performed after such treatment still shows the presence of the rhamnose−phosphonate molecule; the elemental and the energy dispersive spectroscopy (EDS) analysis showed an unchanged Fe/P ratio confirming the absence of rhamnose−phosphonate release after such harsh treatment. Furthermore, the approach used ensures the presence of rhamnose moieties pointing out from the iron oxide NPs, which is an essential requirement for optimum recognition of the appropriate lectin and for cell internalization.

Each step of the synthesis was followed by infrared spectroscopy. The IR spectra of **Rha-4**, **Man-4**, and **Rib-4** display, when compared with the spectrum of the same NPs coated with oleic acid and oleyl amine, the appearance of strong bands at ca. 1750 and 1226 cm^{-1} attributed to the ν(COO) and ν(CO) stretching modes together with the bands at ca. 1080 and at 1050 cm^{-1} assigned to ν(COC) and $\nu(CH_{cycle})$, respectively (see the Supporting Information available, Figure 1S). The band of the ν(P−O−Fe) mode at 1031 cm^{-1} is consistent with the anchoring of the phosphonate moiety to the surface (see the Supporting Information).[39] The characteristic broad envelop at 588 cm^{-1} for **Man-4** and **Rha-4** and at 598 cm^{-1} for **Rib-4**, attributed to ν(Fe−O) bands of iron oxide, indicates that the iron oxide remains intact after sugar anchorage. After deprotection of the sugar acetate groups, the band at ca. 1750 cm^{-1} (ν(COO)) completely disappears, and the intensity of the bands at ca. 1226 cm^{-1} (ν(CO)) are strongly decreased (see the Supporting Information). Consequently, this study highlights the covalent coordination of the sugar derivative via the phosphonate group on the iron oxide surface. Moreover, it confirms the efficient deprotection of sugar acetate groups during treatment in a solution of ammonia/methanol, leading to water-soluble NPs. Note that the change of the NP size does not modify the IR spectra. X-ray photoelectron spectroscopy (XPS) analysis was further used to validate the successful coating of the sugar molecules on the magnetite surface (see the Supporting Information available, Figure 2S).[40]

The transmission electronic microscopy (TEM) measurements performed on the as-obtained NPs show in all cases that they are nonaggregated and uniform. The TEM images of the NPs of **Rha-4**−**Rha-35** samples are shown as an example in Figure 1 (see also the Supporting Information available, Figure 3S, for **Rib-4** and **Man-4** derivatives). Monodisperse NPs of controlled size in the range of 4−35 nm were obtained by varying the synthetic parameters, and the coating process was demonstrated not to modify the morphology, size, or size distribution of the inorganic core (Supporting Information available, Figure 4S). The average size and size distribution obtained from the analysis of a large number of NPs are given in Table 1. A spherical shape is obtained for the 4−18 nm NPs (**Rha-4**−**Rha-18**), while the largest ones (**Rha-35**) present a cubic morphology. Indeed the tendency to assume the more stable cubic habit on decreasing the surface to volume ratio is a well-documented behavior for iron oxide nanoparticles.[41] In all cases the particles exhibit a narrow size distribution. Dynamic light scattering (DLS) shows that the NPs form colloidal solutions in water that are stable over long time periods. The hydrodynamic size determined by this technique are on average ca. 4 nm larger than that obtained by TEM, the difference being ascribed to the sugar layer surrounding the magnetic core. Moreover, the NPs can be suspended in phosphate-buffered saline (PBS) and in physiological solution or in sterile water even at high concentrations forming dispersion stable for long periods.

The powder X-ray diffraction patterns within the 2θ range of 20−70° for **Rha-4**, **Rha-7**, **Rha-10**, and **Rha-35** are given as examples in Figure 2. Similar patterns were obtained for all the investigated samples. The patterns exhibit diffraction peaks which were indexed as (220), (311), (222), (400), (422), (511), and (440) reflections, characteristic of the cubic spinel structure of magnetite and maghemite, or any intermediate composition, which could not be discriminated due to significant line broadening due to the small size of the crystalline domains. As expected the line broadening increases upon decreasing the nanocrystal size. The mean values of the cell parameters obtained by using the Bragg law (see the Supporting Information available) vary between 8.381 (**Rha-4**) and 8.411 Å (**Rha-35**), which is of the same order as the literature value (8.396−8.3515 Å).[42]

The crystalline domain size, determined from the full width at half-height of the most intense peaks, has been calculated using the Debye−Scherrer formula. The values obtained (Table 1) are very similar to those obtained by TEM, which is indicative of crystallographic single domains and high crystallinity of the samples.

Magnetic Properties. The magnetic behavior of the NPs was first investigated by zero field cooled/field cooled experiments, i.e., by measuring the temperature dependence of the magnetization under a 5 mT field after cooling the sample in zero field (ZFC) or with the probe field applied (FC). The magnetic

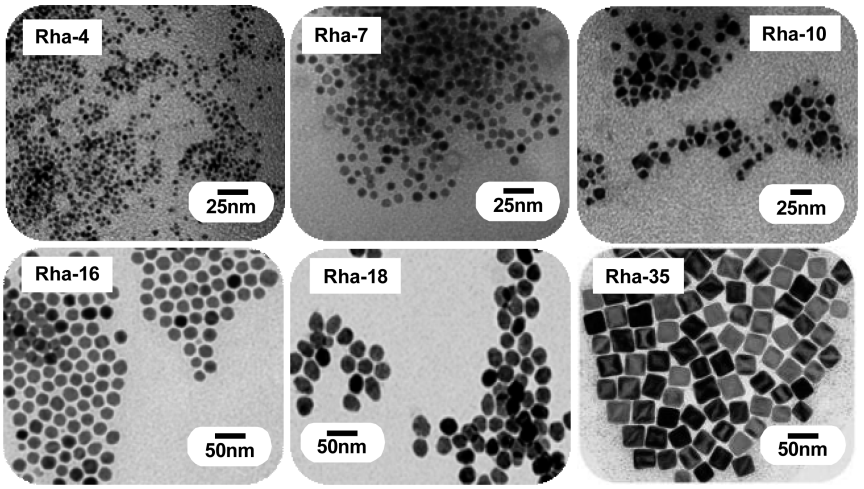

Figure 1. TEM images for NPs of various sizes coated with rhamnose (**Rha-4**−**Rha-35**).

Table 1. Chemical Composition and Average Size of the Core (d) and (d_H) Hydrodynamic Diameters[a]

sample	wt % Fe	wt % iron oxide	wt % P	d [b] (nm)	d [c] (nm)	d_H [d] (nm)	d_{NMR} [e] (nm)
Rha-4	41.9	57.9	4.3	4.1 (0.6)	4.5	8.2 (1.3)	4.6 (0.02)
Rha-7	36.4	50.3	5.0	6.7 (0.8)	6.7	10.4 (1.5)	10.16 (0.04)
Rha-10	29.3	40.5	8.5	10.0 (3.3)	10.9	16.7 (2.6)	10.30 (0.06)
Rha-16	55.6	76.8	2.3	16.2 (1.0)	16.0	21.3 (2.2)	
Rha-18	44.4	61.4	3.9	18.2 (1.1)	18.5	23.6 (2.3)	18.54 (0.03)
Rha-35	55.2	76.3	2.6	35.2 (3.0)	35.4	43.5 (3.3)	

[a] Average diameters were obtained from TEM, XRD, and DLS analyses for rhamnose-coated iron oxide NPs of different sizes (samples **Rha-4**−**Rha-35**). Values in parentheses denote the standard deviations. [b] TEM analysis. [c] XRD analysis. [d] DLS analysis. [e] $d = 2r$ are obtained by fitting the ^{1}H-NMR data.

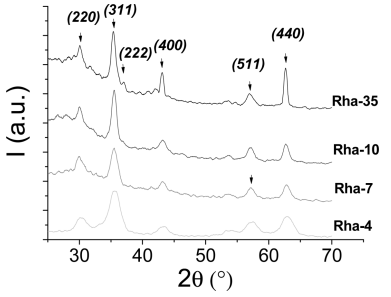

Figure 2. X-ray diffraction patterns within the 2θ range of 20−70° for **Rha-4**, **Rha-7**, **Rha-10**, and **Rha-35**.

properties of the 4 nm NPs coated with different ligands are essentially similar (see the Supporting Information available, Figure 5S), indicating the nature of the sugar does not significantly influence the physical behavior of the inorganic core. Note also that the FC/ZFC curves of the nanoparticles before and after sugar coating are identical. For this reason, in the following discussion we will focus on the investigation of the **Rha-4**−**Rha-35** series only. Figure 3a shows the ZFC/FC magnetization from 2 to 300 K for **Rha-4** and **Rha-16** as representative of the whole series. The ZFC magnetization curves increase with temperature, reaching a maximum at temperature defined as T_{max}. On the contrary, the ZFC curve of sample **Rha-35** (35 nm NPs) increases continuously as the temperature increases and does not show a maximum, suggesting the presence of a ferrimagnetic-like behavior also at room temperature (see the Supporting Information available, Figure 6S). The T_{max} values are plotted in Figure 3b as a function of the average diameter of the NPs and are summarized in Table 2. T_{max} increases continuously with the NPs size but with a d dependence slower (ca. $d^{1.5}$) than the d^3 law predicted by the Néel model for the relaxation of not interacting NPs. The prime cause of behavior is the increasing contribution of the surface to the total effective magnetic anisotropy as d decreases (Figure 4). A similar complex d dependence has been observed in other systems described in the literature: for instance, for noninteracting Fe_3O_4 nanoparticles in the size range of 2.5−14 nm a $d^{1.7}$ law has been observed,[43a] whereas interacting Fe_3O_4 nanoparticles in the range of 7.8−17.9 nm obtained from FeOOH show a quasi linear T_B vs d trend.[43b]

The FC curves of **Rha-4**, **Rha-7**, and **Rha-10** increase as the temperature decreases and never reach saturation at low temperature, suggesting that interparticle interactions do not significantly affect the relaxation dynamics. On the contrary, the FC magnetization of **Rha-16** and **Rha-18** decreases below T_{max} as the temperature decreases, which can be interpreted as the fingerprint of strong magnetostatic interparticle interactions.[44] Accordingly, these features only appear for larger NPs, where the strength of the magnetic interactions is expected to be much greater.

The magnetization as a function of the applied field was measured at room temperature and 2.5 K. The hysteresis loops measured at 300 K display nonzero coercivity (10 mT) only for sample **Rha-35**, confirming that it is largely blocked at room temperature. All of the other samples are in the super-paramagnetic

dx.doi.org/10.1021/ja111448t |J. Am. Chem. Soc. 2011, 133, 10459–10472

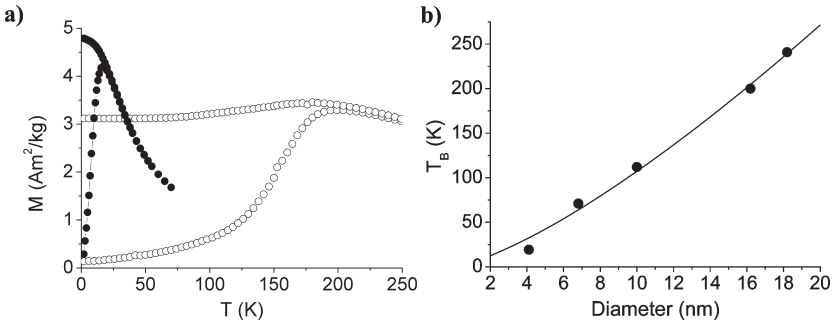

Figure 3. (a) ZFC/FC curves for **Rha-4** (black dots) and **Rha-16** (empty dots) with an applied field of 5 mT; (b) size dependence of T_{max} for samples **Rha-4**−**Rha-18**. The continuous line represents the best fit to a power law.

Table 2. Magnetic Characteristics of Samples Rha-4−Rha-35

					Néel law		Vogel−Fulcher law		
sample	T_{max}(K)	M_S(2.5K) (emu/g)	M_S (300K) (emu/g)	H_C(2K) (mT)	E_a/k_B (K)	τ_0 (s)	E_a/k_B (K)	τ_0 (s)	T_0 (K)
Rha-4	19	96	77	30	337	1.13×10^{-12}	216	9.28×10^{-11}	3
Rha-7	71	94	75	33	1525	1.15×10^{-13}	959	2.24×10^{-11}	12
Rha-10	112	83	70	38	2702	1.28×10^{-12}	2441	6.66×10^{-11}	7
Rha-16	200	82	68	71	9471	1.79×10^{-21}	2020	1.33×10^{-11}	120
Rha-18	241	80	65	100	12260	3.71×10^{-24}	2012	1.16×10^{-11}	150
Rha-35[a]	>300	83	76	54.5					

[a] AC susceptibility data of **Rha-35** were not measured because the sample is blocked at 300 K in the investigated frequency range.

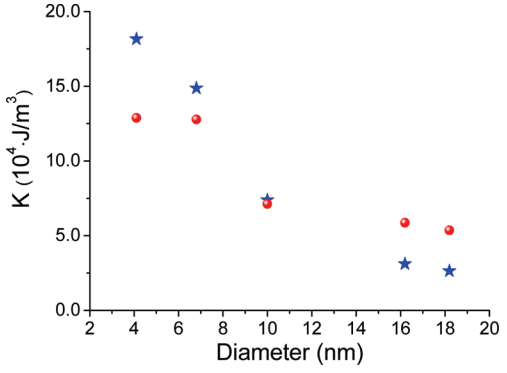

Figure 4. Effective magnetic anisotropy values obtained from E_a (red circles) and T_B (blue stars).

state. The M_S values obtained by extrapolation of the high-field data[45] are reported in Table 2.

Conversely, at low temperature all samples display open hysteretic loops. The coercive field, H_C, reported in Table 2 and shown in Figure 7S (Supporting Information), increases with the average size up to **Rha-18** and then markedly decreases for **Rha-35**. The observed evolution of H_C with the average size agrees well with the empirical model suggested by Hergt et al.,[46] which summarizes the approaches and experimental data reported in the literature over the past few decades:[47] in the pure single-domain regime H_C increases with the size due to the progressively lower efficacy of the thermal demagnetization process; further increase in the size above the super-paramagnetic threshold leads to incoherent reversal mechanisms becoming increasingly favored lowering the field for reversal of the magnetization. Moreover, micromagnetic calculation for cubic NPs in the transition states from single to multidomain, as is the case of **Rha-35**, indicates that flower and vortex magnetic states can further decrease H_C.[48]

The temperature dependence of the in-phase (χ') and out-of-phase (χ'') components of the AC susceptibility were measured for samples **Rha-4**−**Rha-18**. Figure 5a shows the thermal dependence of χ' and χ'' in a zero static field in the 1−1000 Hz range for **Rha-16**, here taken as a representative example. At 1 Hz, χ' and χ'' exhibit peaks at 265 and 247 K, respectively, which shift toward higher temperature with increasing frequency. A similar frequency-dependent behavior was observed for all of the NPs. Depending on the nature and strength of the magnetic interactions, the observed frequency-dependent behavior may be attributed to a blocking−unblocking process for isolated or weakly interacting super-paramagnetic NPs, or to a spin glasslike transition for the case of strongly interacting NPs, as is discussed as follows.[49] According to the Néel model, the temperature dependence of the relaxation of the magnetization of noninteracting super-paramagnetic systems follows an Arrhenius law, $\tau = \tau_0 \exp(E_a/k_B T)$, where E_a is the average energy barrier for magnetization reversal, τ_0 is the attempt time, and k_B is the Boltzmann constant.[50] The best fits of the blocking temperatures obtained from the χ'' maxima for different observation times $\tau = 1/2\pi\nu$ to the Arrhenius law give the E_a and τ_0 values listed in Table 2. Figure 5b shows the Arrhenius law fit for **Rha-16**, as an example. For **Rha-4** and **Rha-10** only, the obtained $\tau_0$values are in the 10^{-8} to 10^{-12} s range typical for isolated nanoparticles in the super-paramagnetic regime.[51] In the other cases, τ_0 is outside this range, indicating the model is not appropriate to describe the dynamics of the systems.[49] Nevertheless, such small $\tau_0$values are usually interpreted as the signature of magnetic moment correlations caused by significant dipole−dipole interparticle interactions.[52] For this reason, the temperature dependence of τ was

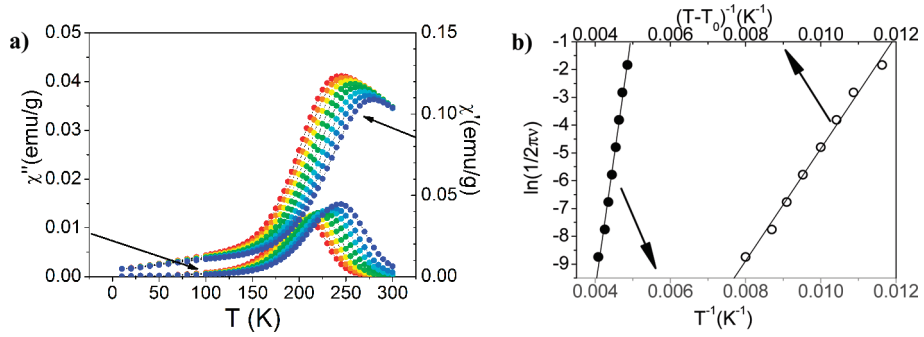

Figure 5. (a) AC susceptibility of sample **Rha-16** performed with various logarithmic spaced frequencies in the 0.1−1000 Hz range. (b) Linear plot of the inverse of maximum temperature of each frequency according to the Arrhenius law (full dots) and according to the Vogel−Fulcher law (empty dots).

also fitted to the Vogel−Fulcher law, $\tau = \tau_0 \exp(E_a/k_B(T - T_0))$, in which an additional parameter T_0 is introduced to take into account the strength of the interparticle interaction. The parameters so obtained are reported in Table 2. As expected for systems where nonnegligible dipolar interactions occur, the Vogel−Fulcher model produces τ_0 values within the proper range and with much lower energy barriers. Moreover, the strong increase of T_0 values indicates that interparticle interactions affect only slightly the magnetization dynamics for **Rha-7**, while, for larger particles (**Rha-16**, **Rha-18**), they cannot be neglected. This conclusion is in agreement with the behavior observed in the ZFC/FC experiments. The consistency of the results obtained from AC and DC techniques is also exemplified by the agreement between the effective anisotropy constant, K, evaluated from the energy barriers, $E_a = KV$, extracted by the Arrhenius plot and from T_B, evaluated as the ZFC curve maxima, assuming $K = 25k_BT_B/V$. The decreasing values of K upon increasing size, which ranges from 12.9×10^4 J/m^3 for **Rha-4** to 5.4×10^4 J/m^3 for **Rha-18** (values from AC measurements) is consistent with the increasing importance of the surface contribution as the particle size is reduced, as mentioned above. The observed K trend can also justify the anomalous T_B vs d dependence (Figure 3b).

Magnetic Hyperthermia Properties. Heat dissipation of ferrofluid produced by the delay in the relaxation of the magnetic moment may be observed when the NPs are exposed to an alternating magnetic field of proper frequency. To experimentally measure this effect, the sample is placed in an alternating magnetic field and the temperature increase is recorded as a function of the application time. The hyperthermal efficiency of a material is normally evaluated by the so-called specific absorption rate, SAR, defined as

$$\mathrm{SAR} = \frac{1}{m_e}\left(\sum_i c_i m_i \frac{dT}{dt}\right) \quad (1)$$

where m_e is the total mass of the iron, c_i is the specific heat of the different species in solution, m_i the weight, and dT/dt the slope of the $T(t)$ curve. Because the experimental setup we used is not perfectly adiabatic (see Experimental Section), the dT/dt value was extrapolated by taking the initial slope of the temperature increase obtained from the linear term of a polynomial fit of the whole curve. The c_i values were taken from the literature,[53] while the m_i values were obtained from elemental analysis. In all cases, a ca. 0.3 g of 10 g·L^{-1} solution is placed in an AC magnetic field of frequency $\nu = 168$ kHz and amplitude $H_0 = 21$ kA/m, corresponding to a product $H_0\nu = 3.5 \times 10^9$ A·m^{-1}·s^{-1}. It should be noted

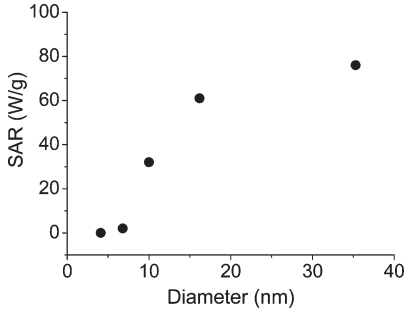

Figure 6. Size dependence of the SAR values measured on water solution with a magnetic field of 168 kHz frequency and 21 kA/m for NPs **Rha-4**−**Rha-35**.

that this value is close to the tolerance threshold limit which, after the experiments by Brezovich et al. on human volunteers, is assumed to be 4.85×10^8 A·m^{-1}·s^{-1}.[54] However, Hergt et al. estimated that for a small exposed region $H_0\nu$ values up to 5×10^9 A·m^{-1}·s^{-1} could be safely applied,[46] and the Jordan group at Berlin's Charité Hospital has exposed human patients to fields of 3.8−13.5 kA/m amplitude and 100 kHz frequency with only minor side effects reported.[55] Larger amplitudes or frequencies can produce tissue heating due to induced eddy currents.

The obtained SAR values are plotted in Figure 6 as a function of particle size.

Clearly, particles with sizes up to 7 nm do not produce significant heating for the experimental conditions adopted. When the size of the NPs exceeds this limit a sudden increase of the SAR value is observed, reaching 76 W/g for **Rha-35**. The SAR can be further increased by increasing the frequency. For example, upon doubling the frequency, the SAR of **Rha-16** changes from 61 to 185 W/g. This value corresponds to an important heating efficiency and, although obtained under conditions slightly above the tolerance limit, makes the material suitable for application as heat mediators for magnetic fluid hyperthermia. Indeed, it is usually accepted that a heat deposition rate of 100 mW·cm^{-3} in tissue is enough to have a sizable effect,[2b] which could be reached for a **Rha-16** concentration between 0.5 and 1.6 g/cm^3, depending on the frequency.

It should be also noted that, although the observed SAR lies in the medium-high range of data reported in the literature to date for maghemite/magnetite MNP,[2f,g] a direct comparison is difficult due to the lack of a clear definition of a protocol for SAR evaluation, which actually requires the control of many environmental parameters. In

fact, for a given NP the SAR should be proportional to the frequency of the AC magnetic field and to the square of its intensity. Even though scaling procedures have been proposed, as for example normalization with respect to the tolerance limit[56] or to $H_0^2\nu$,[57] the lack of accuracy in the calorimetric measurements (dissipation, initial temperature, etc.) can produce significant differences even for samples of very similar composition, morphology, and size. In particular, when the experimental conditions are not perfectly adiabatic, the SAR is always underestimated since its value depends on the thermal dissipation rate, which in turn strongly depends on the environmental temperature.

To rationalize these results, we compare them with the theoretical values estimated using the Rosensweig model[58] for super-paramagnetic NPs:

$$\mathrm{SAR} = \frac{P}{\rho} = 2\pi\nu\frac{\mu_0\chi_0 {H_0}^2}{2\rho}\frac{2\pi\nu\tau}{1+(2\pi\nu\tau)^2} = \pi\nu\frac{V(\mu_0 M_S H_0)^2}{\rho k_B T}\frac{2\pi\nu\tau}{1+(2\pi\nu\tau)^2} \quad (2)$$

where P is the mean volumetric power dissipation, μ_0 is the vacuum magnetic permeability, ρ is the mass density, τ is the relaxation time, and χ_0 is the chord susceptibility; χ_0 is defined as $\mu_0 {M_S}^2 V/(k_B T)L(\xi)/\xi$, V being the average particle volume, k_B the Boltzmann constant, and $L(\xi)$ the Langevin function, where $\xi = \mu_0 M_S V H/(k_B T)$.

Two different mechanisms compete to determine the relaxation of the magnetization: the Néel relaxation, corresponding to the magnetic moment reversal over the energy barrier and characterized by $\tau_N = \tau_0 \exp(KV/k_B T)$, and the Brown relaxation corresponding to the mechanical rotation of the whole particle and described by $\tau_B = 3\eta V_H/k_B T$ (η is the viscosity of the media and V_H is the hydrodynamic volume). The total relaxation time is determined by the fastest process according to $1/\tau = 1/\tau_N + 1/\tau_B$. An evaluation of the SAR for the same conditions used for the calorimetric measurements can then be attempted by use of the hydrodynamic diameters obtained by DLS, namely, τ_B and E_a, and τ_0 obtained from AC measurements using the Néel model for τ_N. The size dependence of Néel, Brown, and total relaxation times for **Rha-4**−**Rha-18** at room temperature is shown in Figure 7. τ_N could not be estimated for **Rha-35** since it has a T_B greater than room temperature.

Comparison of the relaxation times τ_N and τ_B shows that the latter are always longer, so that mechanical rotation is never fast enough to compete with the reversal of the magnetization through the overcoming of the energy barrier. It should be noted that τ_N was evaluated from AC data collected on powder samples while SAR measurements were carried out on water solutions where lower interactions are expected, even though the concentration was high (around 10 mg·mL^{-1}). This is not important for **Rha-4**−**Rha-10**, where interparticle interactions are negligible, but it can affect the relaxation behavior for larger NPs. To gain insight into this point, AC susceptibility measurements on **Rha-16** and **Rha-7** solutions of the same concentration used for magnetothermal experiments were also performed. A fit to an Arrhenius law of the ln τ vs $1/T_{max}$ plot gave energy barriers and τ_0 values close to those obtained with the respective powders (see the Supporting Information available, Table 1S). This suggests that at the high concentrations used for SAR measurements particle aggregation occurs, which can allow for remarkable interactions still being operative.

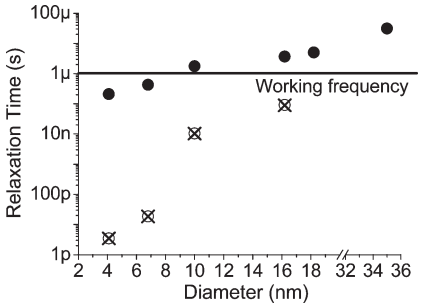

Figure 7. Néel, (○), Brown, (●), and total (×) relaxation times estimated at room temperature in water assuming a viscosity $\eta = 1.003 \times 10^{-3}$ kg·m^{-1}·s^{-1} for samples **Rha-4**−**Rha-18**. For sample **Rha-35,** only τ_B is included because its blocking temperature is greater than room temperature, hampering τ_N evaluation. The solid line represents the time corresponding to the working frequency $\tau = 1/(2\pi\nu)$.

Theoretical SAR values where then estimated using eq 2, where χ_0 is obtained from the room-temperature M_S values and τ from AC powder data. The calculated trend follows that experimentally observed confirming that, for our system in the single-domain regime, the main mechanism for heat release is the relaxation losses due to Néel reorientation. This result can be explained by considering that, on one side, the increase in size induces an increase of the NP magnetic moment and, on the other, it causes the relaxation time to approach the working frequency (see Figure 7). The numerical simulation by Purushotham and Ramanujan,[59] who determined that the size corresponding to the SAR maxima for magnetite NPs is between 19 and 22 nm for a frequency of 100−200 kHz, agrees well with this conclusion.

However, a significant discrepancy between the theoretically and experimentally obtained numerical values is observed. As already pointed out by Rosensweig,[58] the size distribution, which has been neglected to a first approximation, must be taken into account for a more realistic estimate of the SAR value. To assess the importance of the size distribution effect, the SAR was evaluated by replacing $\tau \approx \tau_N(V)$ ($\tau_N \ll \tau_B$) in eq 2 and integrating it over V, whose distribution is considered log-normal with average and standard deviation values reported in column 5 of Table 1. All the other parameters, such as K and M_S, for which a weaker dependence on V is expected, are kept constant. The values obtained, reported in brackets in column 6 of Table 3, are much more reasonable and comparable to those obtained experimentally. As expected,[2g,58] the difference between the two theoretical SAR values highlights the role of the size distribution, which tends to smooth the SAR values, decreasing those which correspond to relaxation times close to the working frequency, **Rha-16**, and increasing those far away, **Rha-10**.

Finally, sample **Rha-35** shows the largest SAR. Since its blocking temperature is well above 300 K, Brownian relaxation is longer than the working frequency and the field amplitude used is larger than the room-temperature coercivity, it can be argued that the mechanism responsible for heat generation is different, as in this case hysteresis losses are predominant. Indeed, even if on a different time scale, a room-temperature minor hysteresis loop between ±25 mT on dry powder shows $H_C = 6.5$ mT and a maximum $M = 0.3M_S$ (see the Supporting Information available, Figure 8S). Therefore, this result suggests that, at least for the field amplitude and frequency used, hysteresis losses are more efficient than super-paramagnetic losses. This behavior is the opposite of that commonly found for iron oxide NPs, where power losses are reported to be largest for sizes between 14 and

Table 3. Relaxation Times and Theoretical and Experimental SAR Values[a]

sample	τ_N	τ_B	τ	$H\nu \times 10^9$ A·m^{-1}·s^{-1}	theoretical SAR W/g	experimental SAR W/g of Fe
Rha-4	3.47×10^{-12}	2.09×10^{-07}	3.47×10^{-12}	3.5	0 (0)	0
Rha-7	1.86×10^{-11}	4.27×10^{-07}	1.86×10^{-11}	3.5	0 (0)	3
Rha-10	1.04×10^{-08}	1.77×10^{-06}	1.03×10^{-08}	3.5	6 (37)	32
Rha-16	9.19×10^{-08}	3.67×10^{-06}	8.97×10^{-08}	3.5	100 (90)	61
				7.0	390 (187)	185
Rha-35		3.13×10^{-05}	$\leq 3.13 \times 10^{-05}$	3.5		76

[a] Columns 2−4 report the Néel, Brown, and total relaxation times estimated as described in the main text. In the fifth column the $H\nu$ product used to measure the SAR is reported, while the two last columns give the experimental and calculated SAR values. Experimental SAR values were obtained using eq 1 with c_{NPs} = 0.67 J/(g·K), c_{water} = 4.18 J/(g·K), and c_{sugar} = 1.2 J/(g·K); m_i values were deduced from the relative weight percentage of particle/sugar found by elemental analysis. Theoretical values were evaluated by eq 2 using the experimentally determined values for M^s and V, and the relaxation times reported in column 4. The values in brackets refer to SAR values determined by taking into account the size distributions as mentioned in the text.

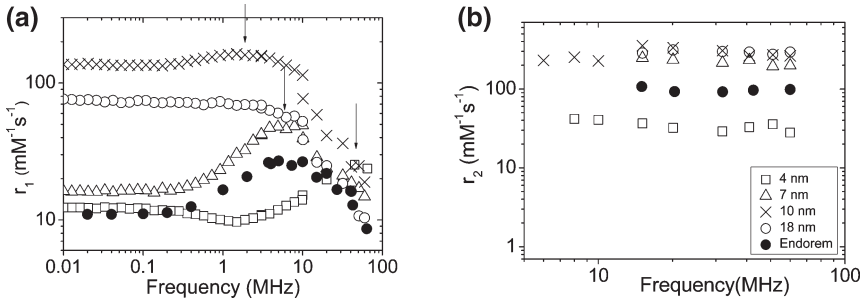

Figure 8. (a) Longitudinal, r_1, and (b) transverse, r_2, relaxivities presented through their NMR-D profile for **Rha4** (□), **Rha-7** (△), **Rha-10** (×) and **Rha-18** (○). For comparison the corresponding data for the commercial contrast agent Endorem (●) are also shown. The arrows indicate the position of the maximum in r_1 for **Rha4**, **Rha7**, and **Rha10**. **Rha-18** displays no maximum due to very high anisotropy.

20 nm [60] and then decrease for larger sizes. Nevertheless, a remarkable exception to this trend was also noted by Hergt et al., who reported an impressive SAR (960 W/g) at 410 kHz and 10 kA/m for monodisperse 38 nm iron oxide bacterial magnetosomes with open hysteresis loops at room temperature.[61] Further investigation of these systems, including an assessment of the SAR dependence on frequency and amplitude and measurements in solvents of different viscosity with a more sensitive experimental apparatus, is required in order to gain a better understanding of this behavior.

In summary, the 16 and 35 nm sugar-coated NPs are the best candidates for hyperthermic applications; however, to be suitable for theranostic purposes a satisfactory relaxometric efficacy is also essential.

Relaxometric Properties. The ^{1}H NMR relaxometry characterization (i.e., NMR dispersion profile) of the samples has been performed at room temperature by measuring the longitudinal and the transverse nuclear relaxation times T_1 and T_2 in the frequency range of 10 kHz ≤ ν ≤ 60 MHz, corresponding to an external magnetic field H = 0.00023−1.5 T.[62] The range was chosen in order to cover the typical fields for MRI tomographs, used both in clinics (H = 0.2, 0.5, and 1.5 T) and research laboratories. It should be noted that the measurements at room and physiological temperatures gave the same results to within 10%.

The relaxivities r_1 and r_2 as function of frequency are reported in Figure 8a,b. For comparison, the values obtained for a commercial super-paramagnetic contrast agent produced by Guerbet Group, i.e., Endorem, have also been plotted. The size dependence of r_2 and of the ratio r_2/r_1 at 1.5 T is given in Figure 9. It is evident that **Rha-7**, **Rha-10**, and **Rha-18** have transverse r_2 relaxivities that are higher than Endorem by a factor as large as 3, over the whole investigated frequency range.

Interestingly, the r_2 value increases upon increasing the core diameter, thus suggesting that the particles are in the so-called "motional averaging regime" (MAR), where water diffusion occurs on a much faster time scale than the resonance frequency shift.[63] With regard to sample **Rha-35**, we observed when the sample was put inside the NMR electromagnet and irradiated with RF pulses to measure T_1 and T_2 values, precipitation occurred after 5−10 min, probably because of the presence of a static magnetic field. Consequently, to ensure that the solution was homogeneous such as in the case of the other samples, sonication before each measurement at different frequency was required. The r_2 values obtained are comparable to those of **Rha-4**. It should be remarked that the precipitation problems observed for **Rha-35** exclude from use in a MRI spectrometer at the clinical level, because of clear risks of thrombosis. Moreover, we should stress that in the hyperthermia measurements no such precipitation was observed, due to the absence of a static magnetic field.

The frequency $r_1(\nu)$ behavior of the investigated samples gives, as usual for super-paramagnetic contrast agents, information on the physical mechanisms that are the main sources of the nuclear relaxation times shortening. First we note that the data for both r_1 and r_2 are consistent with those typical of super-paramagnetic nanostructures,[64−67] where the dimensions of the magnetic core crucially influence the mechanism of relaxation. Second (and as a further confirmation), the behavior of $r_1(\nu)$ is qualitatively the same as the Endorem sample, being represented approximately by the sum of two contributions dominating, respectively, at low (≤1 ÷ 5 MHz) and high (≥1 ÷ 10 MHz) frequencies.[65] At low frequencies, the mechanism driving the nuclear relaxation depends directly on the magnetic anisotropy.

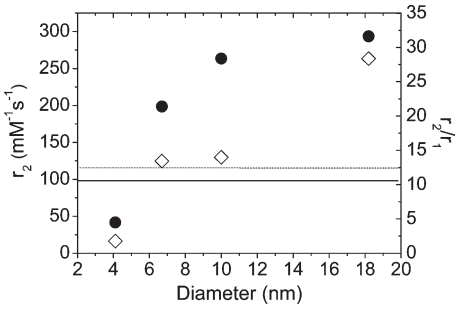

Figure 9. Size dependence of r_2 (●) and the ratio r_2/r_1 (◇) determined at 1.5 T (the most common field applied for medical MRI). The lines represent the r_2 (black line) and r_2/r_1 (dash line) values obtained for Endorem.

At high frequencies, for the smallest particles the nuclear relaxation is dominated by the Curie-relaxation function that takes into account the diffusion of water molecules (with diffusion correlation time $\tau_D = r^2/D$, where r is the distance of closest approach and D the diffusion coefficient of water molecules) in the presence of magnetic centers. On the other hand, the maximum disappears for the compound with the largest diameter.

The experimental data on our samples confirm (as for a few other experimental cases, e.g., refs 66 and 65) qualitatively the predictions of the theory presented by Roch and co-workers.[65] We are currently using this theory to predict the disappearance of the low-frequency dispersion when larger diameters (i.e., higher anisotropy) are considered, to explain the disappearance of the high-frequency maximum in $r_1(\nu)$ for the largest diameter sample, and to estimate the distance r of closest approach to the magnetic core. A first estimate of the NMR diameter obtained in this way, given in Table 1, suggests that the coating of our samples is fully penetrated by the diffusing water molecules. This work is currently in progress and will be published in the near future.

CONCLUSION

In this paper we describe the synthesis of water-dispersible magnetite NPs of different sizes and coated with a crown of sugars. To achieve this goal, we have developed a novel method on the basis of the displacement of oleylamine/oleic acid ligands, used as stabilizers during the synthesis of these NPs, by formation of Fe−O−P bonds between the sugar and the NP via a phosphonate function. A chemical modification of the ligand surface is then performed in an alcoholic medium to remove the acetate protecting groups of the carbohydrates. This methodology is general and has been applied to several sugars. It ensures both an efficient anchoring of the sugar to the NP surface and that the sugar points outward from the NP optimizing the cell recognition capability.

We then conducted a detailed study of the magnetic properties of these NPs, particularly in relation to their relaxivity and magnetic hyperthermia, in order to assess the effect of magnetic core size on the magnetic properties.

The optimum value of SAR obtained for NPs governed by Néel relaxation is 61 $W \cdot g^{-1}$ for a magnetic core size of 16 nm, while it is 76 $W \cdot g^{-1}$ for partially blocked 35 nm NPs. The magnetic field applied in these cases is $H\nu = 3.5 \times 10^9$ $A \cdot m^{-1} \cdot s^{-1}$, which is within the acceptable range limitations imposed by a potential use in the human body. In terms of relaxivity, the NPs **Rha-7**, **Rha-10**, and **Rha-18**, which have a magnetic core greater than 6 nm, display r_2 values greater than the first-generation contrast agent Endorem at fields (frequencies) compatible with clinical use.

Thus, the developed NPs present properties which are interesting for both magnetic resonance imaging and magnetic hyperthermia and have optimum characteristics for inorganic core sizes of ca. 16−18 nm. They are further functionalized with carbohydrates identified as recognition vectors for certain lectins. Therefore, these nanobjects can be regarded as third generation multifunctional sensors for theranostics. Biological studies in vitro and in vivo are currently under way to confirm the potential applications of these nanoprobes. In particular, preliminary cytotoxicity tests by MTT assays has revealed that the MNPs are not toxic, while the first assay on in vitro labeling of melanoma and breast cancer cell lines for **Rha-16**, carried out by the group of Prof. P. Marzola at the University of Verona, Italy, has provided evidence regarding the marked selectivity of our samples. These experiments also proved that the sugar-coating does not significantly increase nonspecific cellular uptake of the particles. All these data will be the subject of a future publication.

ASSOCIATED CONTENT

Supporting Information. Figures showing: FTIR spectra of **Man-4** NP coated by oleic acid and with mannose derivative before and after acetate group deprotection; X-ray photoelectron spectra of sugar-coated magnetite **Rha-16**; TEM images of **Man-4** and **Rib-4**; TEM micrographs of **Rha-4** before and after the removal of the acetate group; ZFC/FC magnetizations of NPs coated with mannose, rhamnose, and ribose derivatives; ZFC/FC of **Rha-35**; coercive field vs NPs diameter for samples **Rha-4**-**Rha**−**35**; minor hysteresis loop recorded at room temperature on a powder of **Rha-35** and a table listing magnetic properties of **Rh-7** and **Rh-16** measured as dry powder and as solution with the same concentration used for hyperthermia experiment. This material is available free of charge via the Internet at http://pubs.acs.org.

AUTHOR INFORMATION

Corresponding Author

yannick.guari@univ-montp2.fr; veronique.montero@univ-montp2.fr; claudio.sangregorio@unifi.it

ACKNOWLEDGMENT

We thank Dr. G. Baldi and Dr. C. Ravagli from Ce.Ri.Col—Colorobbia Italia, C. Rebeil (PAC ICGM, University of Montpellier II, France) for assistance with the calorimetric and magnetic measurements. We thank V. Flaud for XPS measurements and spectrum analysis, the group of M. Borras (CERETOX and Head of the Experimental Toxicology and the ecotoxicology platform of the Barcelona Science Park) for preliminary toxicity measurements, and the group of P. Marzola (University of Verona) for cell-targeting experiments. We are grateful to B. D. Howes for critical reading and improvement of the English text. C.I., T.K., P.A., A.L., D.G., and C.S. gratefully acknowledge the financial support of the EC through NANOTHER (Grant FP7-NMP4-LA-2008-213631). J.L., L.L., Y.G, and C.G. thank the University of Montpellier II and CNRS for

financial support. L.L. thanks the UFI (Grant GF/IR/732/07, No. 25) for financial support.

REFERENCES

(1) (a) Jun, Y.-W.; Lee, J.-H; Cheon, J. *Angew. Chem., Int. Ed.* **2008**, *47*, 5122.(b) Gossuin, Y.; Gillis, P.; Hocq, A.; Vuong, Q. L.; Roch, A. *WIREs Nanomedecine and Nanobiotechnology*; John Wiley & Sons: New York, 2009; Vol. 1 (May/June), p 299.

(2) (a) Gil, P. R.; Parak, W. J. *ACS Nano* **2009**, *2*, 2200. (b) Pankhurst, Q. A.; Connolly, J.; Jones, S. K.; Dobson, J. *J. Phys. D: Appl. Phys.* **2003**, *36*, R167. (c) Cheon, J.; Lee, J.-H. *Acc. Chem. Res.* **2008**, *41*, 1630. (d) Mornet, S.; Vasseur, S.; Grasset, F.; Duguet, E. *J. Mater. Chem.* **2004**, *14*, 2161. (e) Ito, A.; Shinkai, M.; Honda, H.; Lobayashi, T. *J. Biosci. Bioeng.* **2005**, *100*, 1. (f) Goya, G. F.; Grazú, V.; Ibarra, M. R. *Curr. Nanosci.* **2008**, *4*, 1. (g) Fortin, J.-P.; Wilhelm, C.; Servais, J.; Ménager, C.; Bacri, J.-C.; Gazeau, F. *J. Am. Chem. Soc.* **2007**, *129*, 2632.

(3) (a) Hyeon, T. *Chem. Commun. (Cambridge, U. K.)* **2003**, 927.(b) Klabunde, K. J. In *Nanoscale Materials in Chemistry*; Klabunde, K. J., Ed.; Wiley Intersciences: New York, 2001. (c) Diehl, M. R.; Yu, J.-Y.; Heath, J. R.; Doyle, G. A.; Sun, S.; Murray, C. B. *J. Phys. Chem. B* **2001**, *105*, 7913. (d) Leslie-Pelescky, D. L.; Rieke, R. D. *Chem. Mater.* **1996**, *8*, 1770.(e) Schmid, G. *NPs: From Theory to Applications*; Wiley-VCH: Weinheim, Germany, 2004. (f) Niederberger, M.; Garnweitner, G.; Ba, J.; Polleux, J.; Pinna, N. *Int. J. Nanotechnol.* **2007**, *4*, 263. (g) Di Marco, M.; Sadun, C.; Port, M.; Guilbert, I.; Couvreur, P.; Dubernet, C. *Int. J. Nanomed.* **2007**, *2*, 609. (h) Dorman, J. L. *Rev. Phys. Appl.* **1981**, *16*, 275.

(4) Gilchrist, R. K.; Medal, R.; Shorey, W. D.; Hanselman, R. C.; Parott, J. C.; Taylor, C. B. *Ann. Surg.* **1957**, *146*, 596.

(5) (a) Andriola Silva, A. K.; Da Silva, E. L.; Oliveira, E. E.; Nagashima, T.; Soares, L. A. L.; Medeiros, A. C.; Araujo, J. H.; Araujo, I. B.; Carrico, A. S.; Egito, E. S. T. *Int. J. Pharm.* **2007**, *334*, 42. (b) Horáka, D.; Rittichb, B.; Španováb, A. *J. Magn. Magn. Mater.* **2007**, *331*, 249.

(6) (a) Berkovsky, B. M.; Medvedev, V. F.; Krakov, M. S.; *Magnetic Fluids: Engineering Applications*: Oxford University Press: New York, 1993; (b) Rosensweig, R. E.; *Ferrohydrodynamics*; Cambridge University Press: New York, 1985. (c) Kang, Y. S.; Risbud, S.; Rabolt, J. F.; Stroeve, P. *Chem. Mater.* **1996**, *8*, 2209. (d) Massart, R. *IEEE Trans. Magn.* **1981**, *17*, 1247. (e) Massart, R.; Dubois, E.; Cabuil, V.; Hasmonay, E. *J. Magn. Magn. Mater.* **1995**, *149*, 1. (f) Shimoiizaka, J. N. K.; Fujita, T.; Kounosu, A. *IEEE Trans. Magn.* **1980**, *16*, 368. (g) Wooding, A.; Kilner, M.; Lambrick, D. B. J. *Colloid Interface Sci.* **1991**, *144*, 236. (h) Hyeon, T.; Lee, S. S.; Park, J.; Chung, Y.; Na, H. B. *J. Am. Chem. Soc.* **2001**, *123*, 12798. (i) Park, J.; An, K.; Hwang, Y.; Park, J.-G.; Noh, H.-J.; Kim, J.-Y.; Park, J.-H.; Hwang, N.-M.; Hyeon, T. *Nat. Mater.* **2004**, *3*, 891. (j) Euliss, L. E.; Grancharov, S. G.; O'Brien, S.; Deming, T. J.; Stucky, G. D.; Murray, C. B.; Held, G. A. *Nano Lett.* **2003**, *3*, 1489.

(7) (a) De Cuyper, M; Valtonen, S. *J. Magn. Magn. Mater.* **2001**, *225*, 89. (b) Bulte, J. W. M.; de Cuyper, M.; Despres, D.; Frank, J. A. *J. Magn. Magn. Mater.* **1999**, *194*, 204.

(8) Gordon, R. T.; Hines, J. R.; Gordon, D. *Med. Hypotheses* **1979**, *5*, 83.

(9) (a) Jordan, A.; Scholz, R.; Wust, P.; Fahling, H.; Krause, J.; Wlodarczyk, W.; Sander, B.; Vogl, T.; Felix, R. *Int. J. Hyperthermia* **1997**, *13*, 587. (b) Ito, A.; Tanaka, K.; Honda, H.; Abe, S.; Yamaguchi, H.; Kobayashi, T. *J. Biosci. Bioeng.* **2003**, *96*, 364. (c) Jordan, A.; Scholz, R.; Maier-Hauff, K.; van Langeghem, F. K. H.; Waldoefner, N.; Teichgraeber, U.; Pinkernelle, J.; Bruhn, H.; Neumann, F.; Thiesen, B.; Felix, R. *J. Neuro-Oncol.* **2006**, *78*, 7. (d) Hamaguchi, S.; Tohnai, I.; Ito, A.; Mitsudo, K.; Shigetomi, T.; Ito, M.; Honda, H.; Kobayashi, T.; Ueda, M. *Cancer Sci.* **2003**, *94*, 834. (e) Kawai, N.; Ito, A.; Nakahara, Y.; Futakuchi, M.; Shirai, T.; Honda, H.; Kobayashi, T.; Kohri, K. *The Prostate* **2005**, *64*, 373. (f) Le, B.; Shinkai, M.; Kitade, T.; Honda, H.; Yoshida, J.; Wakabayashi, T.; Kobayashi, T. *J. Chem. Eng. Jpn.* **2001**, *34*, 66.

(10) (a) Bulte, J. W.; Kraitchman, D. L. *NMR Biomed.* **2004**, *17*, 484. (b) Michalet, X.; Pinaud, F. F.; Bentolila, L. A.; Tsay, J. M.; Doose, S.; Li, J. J.; Sundaresan, G.; Wu, A. M.; Gambhir, S. S.; Weiss, S. *Science* **2005**, *307*, 538. (c) Couvreur, P.; Vauthier, C. *Pharm. Res.* **2006**, *23*, 1417. (d) Weissleder, R. R. P. *Eur. Radiol.* **1993**, *3*, 198.

(11) Rinck, P. A., Ed. *Magnetic Resonance in Medicine*, 3rd ed.; Blackwell: Oxford, U.K., 1993.

(12) (a) Geraldes, C. F. G. C.; Laurent, S *Contrast Media Mol. Imaging* **2009**, *4*, 1. (b) Corot, C.; Robert, Ph.; Idée, J.-M.; Port, M. *Adv. Drug Delivery Rev.* **2006**, *58*, 1471. (c) Weissleder, R.; Stardk, D. D.; Engelastad, B. L.; Bacon, B. R.; Compton, C. C.; White, D. L.; Jacobs, P.; Lewis, J. *Am. J. Roentgenol.* **1989**, *152*, 167. (d) Reimer, P.; Rummeny, E. J.; Daddrup, H. E.; Balzer, T.; Tombach, B.; Berns, T.; Peters, P. E. *Radiology* **1995**, *195*, 489. (e) Jung, C. W.; Jacobs, P. *Magn. Reson. Imaging* **1995**, *13*, 661. (f) Josephson, L.; Tung, C.-H.; Moore, A.; Weissleder, R. *Bioconjugate Chem.* **1999**, *10*, 186. (g) Weissleder, R.; Lee, A. S.; Fischman, A. J.; Reimer, P.; Shen, T.; Wilkinson, R.; Callahan, R. J.; Brady, T. J. *Radiology* **1991**, *181*, 245.

(13) (a) Jun, Y.-W.; Huh, Y.-M.; Choi, J.-s.; Lee, J.-H.; Song, H.-T.; Kim, S.; Yoon, S.; Kim, K.-S.; Shin, J.-S.; Suh, J.-S.; Cheon, J. *J. Am. Chem. Soc.* **2005**, *127*, 5732. (b) Huh, Y.-M.; Jun, Y.-w.; Song, H.-T.; Kim, S.; Choi, J.-s.; Lee, J.-H.; Yoon, S.; Kim, K.-S.; Shin, J.-S.; Suh, J.-S.; Cheon, J. *J. Am. Chem. Soc.* **2005**, *127*, 12387. (c) Jun, Y.-W.; Seo, J.-W.; Cheon, J. *Acc. Chem. Res.* **2008**, *41*, 179. (d) Na, H.-B.; Song, I.-C.; Hyeon, T. *Adv. Mater.* **2009**, *21*, 2133. (e) Yang, H.-M.; Lee, H.-J.; Jang, K.-S.; Park, C. W.; Yang, H. W.; Heo, W. D.; Kim, J.-K. *J. Mater Chem.* **2009**, *19*, 4566. (f) Tromsdorf, U. I.; Bigall, N. C.; Kaul, M. G.; Bruns, O. T.; Nikolic, M. S.; Mollwitz, B.; Sperling, R. A.; Reimer, R.; Hohenberg, H.; Parak, W. J.; Förster, S.; Beisigel, U.; Adam, G.; Weller, H. *Nano Lett.* **2007**, *7*, 2422. (g) Boni, A.; Marinone, M.; Innocenti, C.; Sangregorio, C.; Corti, M.; Lascialfari, A.; Mariani, M.; Orsini, F.; Poletti, G.; Casula, M. F. *J. Phys. D: Appl. Phys.* **2008**, *41*, 134021. (f) Lee, H.-Y. *Nanotechnology* **2008**, *19*, 165101. Figuerola, A.; Fiore, A.; Di Corato, R.; Falqui, A.; Giannini, C.; Micotti, E.; Lascialfari, A.; Corti, M.; Cingolani, R.; Pellegrino, T.; Cozzoli, P. D.; Manna, L. *J. Am. Chem. Soc.* **2008**, *130*, 1477. Corti, M.; Lascialfari, A.; Micotti, E.; Castellano, A.; Donativi, M.; Quarta, A.; Cozzoli, P. D.; Manna, L.; Pellegrino, T.; Sangregorio, C. *J. Magn. Magn. Mater.* **2008**, *320*, e320.

(14) (a) Rochenbertger, J.; Sher, E. C.; Alivsatos, A. P. *J. Am. Chem. Soc.* **1999**, *121*, 11595. (b) Sun, S. H.; Zeng, H.; Robinson, D. B.; Raoux, S.; Rice, P. M.; Wang, S. X.; Li, G. X. *J. Am. Chem. Soc.* **2004**, *126*, 273. (c) Park, J.; An, K.; Hwang, Y.; Park, J.-G.; Hoh, H.-J.; Kim, J.-Y.; Park, J.-H.; Hwang, N.-M.; Hyeon, T. *Nat. Mater.* **2004**, *3*, 891. (d) Jana, N. R.; Chen, Y.; Peng, X. *Chem. Mater.* **2004**, *16*, 3931. (e) Jun, Y.; Choi, J.; Cheon, J. *Chem. Commun. (Cambridge, U. K.)* **2007**, 1203. (f) Cheon, J.; Kang, N.-J.; Lee, S.-M.; Yoon, J.-H.; Oh, S. J. *J. Am. Chem. Soc.* **2004**, *126*, 1950. (g) Lu, A.-H.; Salabas, E. L.; Schüth, F. *Angew. Chem., Int. Ed.* **2007**, *46*, 1222. (h) Shevchenko, E. V.; Talapin, D. V.; Rogach, A. L.; Kornowski, A.; Hasse, M.; Weller, H. *J. Am. Chem. Soc.* **2002**, *124*, 11480. (i) Tracy, J. B.; Weiss, D. N.; Dinega, D. P.; Bawendi, M. G. *Phys. Rev. B* **2005**, *72*, 064404. (j) Sun, S. *Adv. Mater.* **2006**, *18*, 393. (k) Puntes, V. F.; Krishnan, K. M.; Alivisatos, A. P. *Science* **2001**, *291*, 2115. (l) Song, Q.; Zhang, Z. J. *J. Am. Chem. Soc.* **2004**, *126*, 6164. (m) Tan, Y.; Zhuang, Z.; Peng, Q.; Li, Y. *Chem. Mater.* **2008**, *20*, 5029.

(15) Yang, J.; Lee, T. I.; Lim, E.-K.; Hyung, W.; Lee, C.-H.; Song, Y. J.; Suh, J.-S.; Yoon, H.-G.; Huh, Y.-M.; Haam, S. *Chem. Mater.* **2007**, *19*, 3870.

(16) Renshaw, P. F.; Owen, C. S.; McLaughlin, A. C.; Frey, T. G.; Leigh, J. S. *Magn. Reson. Med.* **1986**, *3*, 217.

(17) (a) Yang, X.; Chen, Y.; Yuan, R.; Chen, G.; Blanco, E.; Gao, J.; Shuai, X. *Polymer* **2008**, *49*, 3477. (b) Shi, X.; Wang, S. E.; Swanson, S. D.; Ge, S.; Cao, Z.; Van Antwerp, M. E.; Landmark, K. J.; Baker, J. R., Jr. *Adv. Mater.* **2008**, *20*, 1671. (c) Wang, S. H.; Shi, X.; Van Antwerp, M.; Cao, Z.; Swanson, S. D.; Bi, X.; Baker, J. R., Jr. *Adv. Mater.* **2007**, *17*, 3043.

(18) (a) Shen, T.; Weissleder, R.; Papisov, M.; Bogdanov, A.; Brady, T. J. *Magn. Reson. Med.* **1993**, *29*, 599. (b) Reimer, P.; Jahnke, N.; Schima, M.; Deckers, F.; Marx, F.; Holzknecht, N.; Saini, S. *Radiology* **2000**, *217*, 152. (c) Zhao, M.; Kircher, M. F.; Josephson, L.; Weissleder, R. *Bioconjugate Chem.* **2002**, *13*, 840.

(19) (a) Thunemann, A. F.; Schutt, D.; Kaufner, L.; Pison, U.; Mohwald, H. *Langmuir* **2006**, *22*, 2351. (b) Jain, T. K.; Morales, M. A.;

Sahoo, S. K.; Leslie-Pelecky, D. L.; Labhasetwar, V. *Mol. Pharmaceutics* **2005**, *2*, 194.
(20) Kim, D. K.; Mikhaylova, M.; Wang, F. H.; Kehr, J.; Bjelke, B.; Zhang, Y.; Tsakalakos, T.; Muhammed, M. *Chem. Mater.* **2003**, *15*, 4343.
(21) Huh, Y.-M.; Jun, Y.-W.; Song, H.-T.; Kim, S.; Choi, J.-S.; Lee, J.-H.; Yoon, S.; Kim, K.-S.; Shin, J.-S.; Suh, J.-S.; Cheon, J. *J. Am. Chem. Soc.* **2005**, *127*, 12387.
(22) Yigit, M. V.; Mazumdar, D.; Lu, Y. *Bioconjugate Chem.* **2008**, *19*, 412.
(23) Xie, J.; Chen, K.; Lee, H.-Y.; Xu, C.; Hsu, A. R.; Peng, S.; Chen, X.; Sun, S. *J. Am. Chem. Soc.* **2008**, *130*, 7542.
(24) Weissleder, R.; Moore, A.; Mahmood, U.; Bhorade, R.; Benveniste, H.; Chiocca, E. A.; Basilion, J. P. *Nat. Med.* **2000**, *6*, 351.
(25) Lee, Y. C., Lee, R. T., Eds. *Neoglycoconjugates: Preparation and Applications*; Academic Press: New York, 1994.
(26) El-Boubbou, K.; Zhu, D. C.; Vasileiou, C.; Borhan, B.; Prosperi, D.; Li, W.; Huang, X. *J. Am. Chem. Soc.* **2010**, *132*, 4490.
(27) Barragan, V.; Menger, F. M.; Caran, K.; Vidil, C.; Morere, A.; Montero, J.-L. *Chem. Commun. (Cambridge, U. K.)* **2001**, *1*, 85.
(28) Shimomura, M.; Ono, B.; Oshima, K.; Miyauchi, S. *Polymer* **2006**, *47*, 5785.
(29) El-Boubbou, K.; Gruden, C.; Huang, X. *J. Am. Chem. Soc.* **2007**, *129*, 13393.
(30) Astete, C. E.; Kumar, C. S. S. R.; Sabilov, C. M. *Colloids Surf., A* **2007**, *299*, 209.
(31) Horac, D.; Babic, M.; Jendelova, P.; Herynek, V.; Trchova, M.; Pientka, Z.; Pollert, E.; Sykova, E. *Bioconjugate Chem.* **2007**, *18*, 635.
(32) Lartigue, L.; Oumzil, K.; Guari, Y.; Larionova, J.; Guérin, Ch.; Montero, J.-L.; Barragan-Montero, V.; Sangregorio, C.; Caneschi, A.; Innocenti, C.; Kalaivani, T.; Arosio, P.; Lascialfari, A. *Org. Lett.* **2009**, *11*, 2992.
(33) (a) Barragan-Montero, V.; Winum, J.-Y.; Molès, J.-P.; Juan, E.; Clavel, C.; Montero, J.-L. *Eur. J. Med. Chem.* **2005**, *40*, 1022.(b) Barragan, V. ; Montero, J.-L. ; Winum, J.-Y. ; Juan, E. ; Moles, J.-P. French Patent FR 2854896, 2007.
(34) Taylor, P. R.; Gordon, S.; Martinez-Pomares, L. *Trends Immunol.* **2005**, *26*, 104.
(35) Hou, Y.; Xu, Z.; Sun, S. *Angew. Chem., Int. Ed.* **2007**, *46*, 6329.
(36) (a) Yu., W. W.; Falkner, J. C.; Yazuz, C. T.; Colvin, V. L. *Chem. Commun. (Cambridge, U. K.)* **2004**, 2306. (b) Lin, C.-R.; Chiang, R.-K.; Wang, J.-S.; Sung, T.-W. *J. Appl. Phys.* **2006**, *99*, 08N710.
(37) Michaëlis, A.; Becker, T. *Chem. Ber.* **1897**, *30*, 1003.
(38) Montero, J.-L.; Imbach, J.-L. *Eur. J. Med. Chem.* **1982**, *17*, 97.
(39) (a) Mohapatra, S.; Pramanik, P. *Colloids Surf., A* **2009**, *339*, 35. (b) Guerrero, G.; Mutin, P. H. A. *Chem. Mater.* **2001**, *13*, 4367.
(40) Das, M.; Mishra, D.; Dhak, P.; Gupta, S.; Maiti, T. K.; Basak, A.; Prarmanik, P. *Small* **2009**, *5*, 2883.
(41) (a) Kovalenko, M. V.; Bodnarchuk, M. I.; Lechner, R. T.; Hesser, G.; Schäffler, F.; Heiss, W. *J. Am. Chem. Soc.* **2007**, *129*, 6352. (b) Shavel, A.; Rodriguez-Gonzalez, B.; Spasova, M.; Farle, M.; Liz-Marzan, L. M. *Adv. Funct. Mater.* **2007**, *17*, 3870. (c) Shavel, A.; Rodriguez-Gonzalez, B.; Pacifico, M.; Spasova, M.; Farle, M.; Liz-Marzan, L. M *Chem. Mater.* **2009**, *21*, 1326.
(42) Fleet, M. E. *Acta Crystallogr.* **1981**, *B37*, 917.
(43) (a) Demortière, Panissod, P.; Pichon, B. P.; Pourroy, G.; Guillon, D.; Donnio, B.; Egin- Colin, S. B. *Nanoscale* **2011**, *3*, 225. (b) Lin, C.-R.; Chiang, R.-K.; Wang, J. S.; Sung, T. W. *J. Appl. Phys.* **2006**, *99*, 08N710.
(44) D. Parker, D.; Dupuis, V.; Ladieu, F.; Bouchaud, J.-P.; Dubois, E.; Perzynski, R.; Vincent, E. *Phys. Rev. B* **2008**, *77*, 104428.
(45) Morrish, A. H. *The Physical Principles of Magnetism*; John Wiley & Sons: New York, 1965.
(46) Hergt, R.; Dutz, S.; Röder, M. *J. Phys.: Condens. Matter* **2008**, *20*, 385214.
(47) (a) Kneller, E. F.; Luborsky, F. E. J. *Appl. Phys.* **1963**, *34*, 656. (b) Cullity, B. D. *Introduction to Magnetic Materials*; Addison-Wesley: Reading, MA, 1972.
(48) Fabian, K.; Kirchner, A; Williams, W.; Heider, F.; Leib, T.; Huber, A. *Geophys. J. Int.* **1996**, *124*, 89.
(49) Folch, J.; Larionova, J.; Guari, Y.; Molvinger, K.; Luna, C.; Sangregorio, C.; Innocenti, C.; Caneschi, A.; Guérin, Ch. *Phys. Chem. Chem. Phys.* **2010**, *12*, 12760–12770.
(50) Néel, L. *Ann. Geophys.* **1949**, *5*, 99.
(51) Chikazumi, S. *Physics of Ferromagnetism*, 2nd ed.; Clarendon: Oxford, U.K., 1997.
(52) Djurberg, C.; Svedlindh, P.; Nordblad, P.; Hansen, M. F.; Bodker, F.; Morup, S. *Phys. Rev. Lett.* **1997**, *79*, 5154.
(53) Weast, R. C., Ed. *Handbook of Chemistry and Physics*, 53rd ed.; CRC Press: Cleveland, OH, 1972; p D-128.
(54) Atkinson, W. J.; Brezovich, I. A.; Chakraborty, D. P. *IEEE Trans. Biomed. Eng.* **1984**, *31* (BMEE), 70.
(55) Maier-Hauff, K.; Rothe, R.; Scholz, R.; Gneveckow, U.; Wust, P.; Thiesen, B.; Feussner, A.; von Deimling, A.; Waldoefner, N.; Felix, R.; Jordan, A. *J. Neuro-Oncol.* **2007**, *81*, 53–60.
(56) Andrä, W., Nowak, H., Eds. *Magnetism in Medicine. A Handbook*; Wiley-VCH Verlag: Berlin, 1998.
(57) (a) Chan, D. C. F.; Kirpotin, D. B.; Bunn, P. A. *Scientific and Clinical Applications of Magnetic Carriers*; Hafeli, U., Ed.; Plenum Press: New York, 1997; pp 607−618. (b) Kallumadil, M.; Tada, M.; Nakagawa, T.; Abe, M.; Southern, P.; Pankhurst, Q. A. *J. Magn. Mater.* **2009**, *321*, 1509.
(58) Rosensweig, R. E. *J. Magn. Mater.* **2002**, *252*, 370.
(59) Purushotham, S.; Ramanujan, R. V. *J. Appl. Phys.* **2010**, *107*, 114701.
(60) Okawa, K.; Sekine, M.; Maeda, M.; Tada, M.; Abe, M.; Matsushita, N.; Nishio, K.; Handa, H. *J. Appl. Phys.* **2006**, *99*, 08H102.
(61) Hergt, R.; Hiergeist, R.; Zeisberger, M.; Schuler, D.; Heyen, U.; Hilger, I.; Kaiser, W. A. *J. Magn. Mater.* **2005**, *293*, 80.
(62) Ferrante, G.; Sykora, S. *Adv. Inorg. Chem.* **2005**, *57*, 405.
(63) Gillis, P.; Moiny, F.; Brooks, R. A. *Magn. Reson. Med.* **2002**, *47*, 257. Yablonskiy, D. A.; Haacke, E. M. *Magn. Reson. Med.* **1994**, *32*, 749.
(64) (a) Bulte, J. W. M.; Vymazal, J.; Brooks, R. A.; Pierpaoli, C.; Frank, J. A. *J. Magn. Reson. Imaging* **1993**, *3*, 641.(b) Bulte, J. W. M.; Brooks, R. A. *Scientific and Clinical Applications of Magnetic Carriers*; Häfeli, U., Ed.; Plenum Press: New York, 1997; pp 527−542.
(65) Roch, A.; Muller, R. N.; Gillis, P. *J. Chem. Phys.* **1999**, *110*, 5403.
(66) Boni, A.; Marinone, M.; Innocenti, C.; Sangregorio, C.; Corti, M.; Lascialfari, A.; Mariani, M.; Orsini, F.; Poletti, G.; Casula, M. F. *J. Phys. D: Appl. Phys.* **2008**, *41*, 134021.
(67) Casula, M. F.; Floris, P.; Innocenti, C.; Lascialfari, A.; Marinone, M.; Corti, M.; Sperling, R. A.; Parak, W. J.; Sangregorio, C. *Chem. Mater.* **2010**, *22*, 1739.